

# Non-classical optimization through complex media

Baptiste Courme,<sup>1,2</sup> Chloé Vernière,<sup>1</sup> Malo Joly,<sup>2</sup> Daniele Faccio,<sup>3</sup> Sylvain Gigan,<sup>4</sup> and Hugo Defienne<sup>1</sup>

<sup>1</sup>*Sorbonne Université, CNRS, Institut des NanoSciences de Paris, INSP, F-75005 Paris, France*

<sup>2</sup>*Laboratoire Kastler Brossel, ENS-Université PSL, CNRS,*

*Sorbonne Université, Collège de France, 24 rue Lhomond, 75005 Paris, France*

<sup>3</sup>*School of Physics and Astronomy, University of Glasgow, Glasgow G12 8QQ, UK*

<sup>4</sup>*Laboratoire Kastler Brossel, ENS-Université PSL, CNRS,*

*Sorbonne Université, Collège de France, 24 rue Lhomond, 75005 Paris, France*

(Dated: April 1, 2025)

Optimization approaches are ubiquitous in physics. In optics, they are key to manipulating light through complex media, enabling applications ranging from imaging to photonic simulators. In most demonstrations, however, the optimization process is implemented using classical coherent light, leading to a purely classical solution. Here we introduce the concept of optical non-classical optimization in complex media. We experimentally demonstrate the control and refocusing of non-classical light - namely, entangled photon pairs - through a scattering medium by directly optimizing the output coincidence rate. The optimal solutions found with this approach differ from those obtained using classical optimization, a result of entanglement in the input state. Beyond imaging, this genuinely non-classical optimization method has potential to tackle complex problems, as we show by simulating a spin-glass model with multi-spin interactions.

## I. INTRODUCTION

In 2007, Vellekoop and Mosk demonstrated the focusing of classical coherent light through opaque scattering media [1]. They developed an optimization process that tailors the wavefront of a coherent beam incident on the medium using a spatial light modulator (SLM), based on a speckle intensity feedback measured by a camera behind it (Figs. 1a-d). Two decades later, this breakthrough has led to numerous applications in deep-tissue imaging [2, 3], light transport in multimode fibers [4], optical trappings [5] and complex problems simulation [6, 7]. In recent years, it was also extended to quantum optics [8]. Pioneering studies have, for example, reported the focusing of single photons and photon pairs through thick scattering media [9–11] and multimode fibers [12, 13]. These approaches have subsequently been applied to more practical scenarios, such as programming quantum circuits [14–16], imaging through optical aberrations [17], and restoring entanglement after transmitting photons through fibers [18], scattering layers [19–22] and turbulent atmosphere [23–25].

Although all these studies involve non-classical optical states, they still rely on classical wavefront shaping. Indeed, in most of them, wavefront optimization is performed first using a classical light source - a laser aligned in the same direction as the quantum state, sharing similar spectral and polarization properties - before applying the optimal solution to the quantum signal. This method benefits from an intense signal for optimization, which is particularly useful in high-loss scenarios (e.g. multiple scattering) and dynamic conditions (e.g. turbulence) [1, 26, 27]. However, it completely ignores the non-classical features of the quantum state involved, making the process purely classical.

Ignoring the quantum state's specifics in the shaping process has its limits. Practically, ensuring perfect

mode matching between a classical and a non-classical source is often challenging. For example, in the context of high-dimensional entangled states, such as spatially entangled photon pairs [28], scattering has only been corrected either simultaneously for a small subset of modes [20, 21, 29] or sequentially by addressing each mode individually [15, 18]. More importantly, it fundamentally restricts the efficiency and range of the control achieved. Purely non-classical phenomena, such as complex quantum interference [16, 30] and entanglement scrambling [18, 21], for example, are not taken into account when using classical optimization.

Here, we present an optimization-based wavefront shaping method with direct feedback from a non-classical feature of a quantum state - non-classical optimization - leading to solutions unattainable through classical optimization. Our experimental implementation involves an entangled two-photon state propagating through a scattering medium. Contrary to previous works, the feedback signal is derived directly from photon coincidence measurements across spatial modes at the output, which are specific to the non-classical source. To better understand this behavior, we investigate the two-photon interference processes occurring in the scattering medium and develop an analytical model for the spatial correlation modulation. We demonstrate that the optimization converges towards unique solutions which do not refocus classical light. Crucially, we show that these non-classical solutions exist and are accessible only if entanglement is present between the photons. Finally, we highlight the potential of such non-classical optimization for solving computationally hard problems by mapping it to a spin-glass optical simulator with multi-spin interactions.

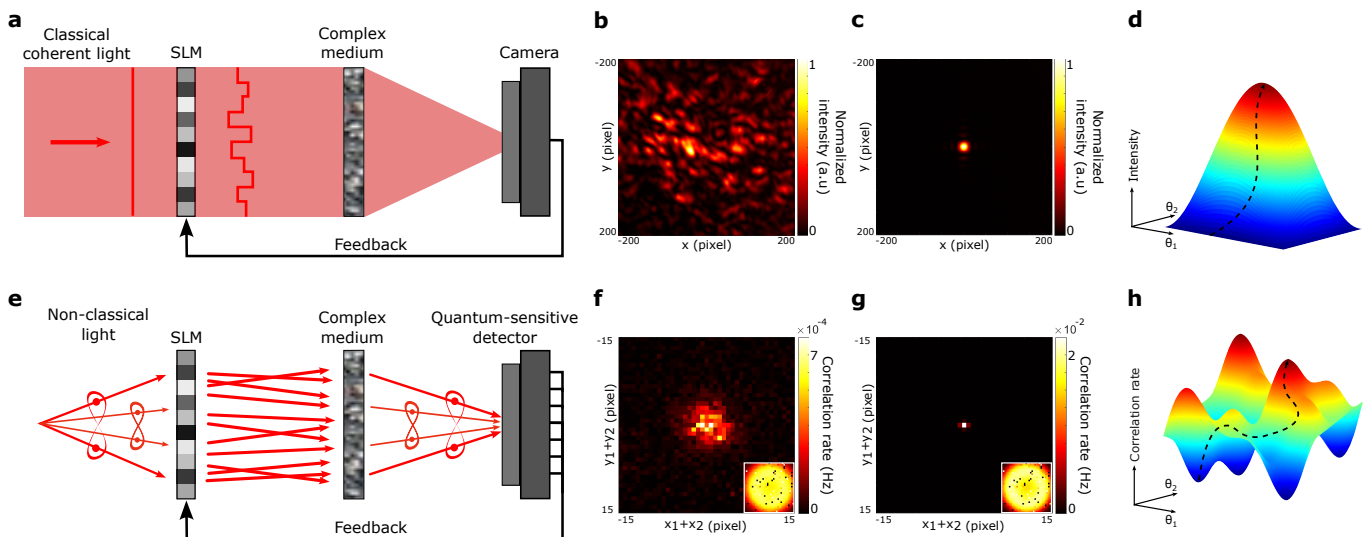


Figure 1. **Classical and non-classical optimizations.** **a**, Refocusing classical coherent light through a complex medium is achieved by optimization-based wavefront shaping, as described in Ref. [1]. A feedback loop is established between the intensity of the output speckle pattern, measured by a camera, and a spatial light modulator (SLM) that shapes the wavefront of the incident beam. This iterative optimization increases intensity at the target spatial mode, effectively correcting distortions introduced by the medium. **b and c**, Intensity images measured before and after optimization, respectively. **d**, Optimization landscape showing a unique maximum, where  $\theta_1$  and  $\theta_2$  represent the phases of two SLM pixels. **e**, In non-classical optimization, a feedback loop is established between a non-classical property of the quantum state measured at the output and a shaping device at the input. This loop iteratively adjusts the input shaping to enhance the targeted non-classical property. In our experiment, non-classical optimization is implemented using spatially-entangled photon pairs propagating through a scattering medium and detected in coincidence using a single-photon avalanche diode (SPAD) camera. Photons are strongly correlated in their momentum i.e. between  $\mathbf{k}$  and  $-\mathbf{k}$ . **f**, Before optimization, the sum-coordinate projection of  $\Gamma$  exhibits a speckle pattern, while the intensity is uniform (inset). **g**, If the optimization is successful, a peak emerges in the projection of  $\Gamma$ , confirming the restoration of strong spatial correlations between the photons, while the intensity remains uniform (inset). **h**, Optimization landscape showing multiple local maxima, where  $\theta_1$  and  $\theta_2$  represent the phases of two SLM pixels.

## II. CONCEPT

Figures 1 conceptually compares classical and non-classical optimization. A non-classical state propagates through a complex medium and is measured at the output by a detector sensitive to its quantum properties, such as a single-photon or homodyne detector. A feedback mechanism is then implemented, linking this measurement to a programmable device that shapes the properties of the state incident on the medium. An iterative algorithm adjusts the input (usually the spatial phase pattern) towards a configuration that optimizes the targeted non-classical property.

In our work, non-classical optimization is demonstrated using a spatially-entangled two-photon state propagating through a scattering layer and detected by a single-photon avalanche diode (SPAD) camera. At the input, the state has strong multimode spatial correlations: when a photon is detected in any transverse spatial mode  $\mathbf{k}$ , its twin has a high probability of being detected precisely in the symmetric mode  $-\mathbf{k}$  [28]. At the output, the SPAD camera detects photons across all spatial modes in parallel, enabling measurement of both the intensity image (single counts) and the spatially-resolved second order correlation function  $\Gamma$  (coincidence

counts) [31]. After propagation, the intensity remains uniform, but a speckle pattern appears in the sum-coordinate projection  $\Gamma$  (Fig. 1f). This speckle results from complex two-photon interference [32] and indicates a degradation of the initial strong spatial correlation between the photons. The correlation value between any arbitrary pair of pixels is chosen as the optimization target, and a feedback loop is implemented with a SLM that modulates the wavefront of the input state. If the optimization is successful, a peak emerges in the projection of  $\Gamma$  (Fig. 1g).

## III. OPTIMIZATION

When a pure two-photon state propagates through a linear scattering medium, the coincidence rate  $\Gamma_{kl}$  between two output modes  $k$  and  $l$  can be expressed as

$$\Gamma_{kl} = \left| \sum_{m,n} t_{km} t_{ln} \psi_{mn}^{(i)} e^{i\theta_{nm}} \right|^2, \quad (1)$$

where  $\psi_{mn}^{(i)}$  is the input two-photon field decomposed over the input modes  $m$  and  $n$ ,  $t_{kn}$  is a scattering matrix coefficient linking input mode  $n$  to output mode  $k$ , and  $\theta_{nm}$

are adjustable phase terms. In our study, we consider only spatial modes (photons have the same frequency and polarization), though the problem can generalize to all degrees of freedom. It is clear that a maximum value of  $\Gamma_{kl}$  is reached when all the terms in equation 1 are in phase i.e. when all  $\theta_{nm}$  are carefully adjusted to cancel the phase of  $t_{km}t_{ln}\psi_{mn}^{(i)}$ . This problem is analogous to the classical optimization problem detailed in Ref. [1], which is well known to have a unique solution (up to a global phase) with only a global maximum and no local minima, as shown in Fig. 1 and demonstrated in supplementary section I. See also Methods for details on equation (1).

For coincidence optimization, unlike the classical case, a single SLM does not have enough degrees of freedom to independently control all the  $\theta_{nm}$  and perfectly align all the terms in equation 1. For instance, considering only two spatial input modes (SLM pixels  $m$  and  $n$ ) and two spatial output modes (camera pixels  $k$  and  $l$ ), three terms corresponding to four two-photon paths must be put in phase:  $t_{km}t_{lm}\psi_{mm}^{(i)}e^{2i\theta_m}$  (Fig. 2a),  $t_{ln}t_{kn}\psi_{nn}^{(i)}e^{2i\theta_n}$  (Fig. 2b) and  $(t_{kn}t_{lm}+t_{km}t_{ln})\psi_{mn}^{(i)}e^{i(\theta_m+\theta_n)}$  (Figs. 2c and d), where  $\theta_m$  and  $\theta_n$  are phase shifts applied to modes  $n$  and  $m$ . When considering  $N > 2$  input modes, the optimization problem thus becomes finding a set of phases  $\{\theta_n\}$ ,  $n \in [1, N]$ , that optimally adjusts the  $N^2$  phases  $\theta_{nm}$  to maximize the coincidence rate between the target output modes. This optimization problem is significantly more complex than its classical counterpart. For instance, simple simulations shown in Figure 1h and in supplementary section II demonstrate the presence of local maxima and clearly indicate that the optimal solution is not always unique.

To tackle this problem, we have adapted an iterative optimization approach derived from the random partition algorithm [33]. At each step, a subset of SLM pixels are selected and shifted (active SLM area) relative to another part that remains flat (reference SLM area). The two-photon speckle fields interfere at the output, causing the target coincidence rate  $\Gamma_{kl}$  to vary as

$$\Gamma_{kl}(\theta) = A \cos(2\theta + \theta_A) + B \cos(\theta + \theta_B) + C, \quad (2)$$

where  $A$ ,  $B$ ,  $C$ ,  $\theta_A$ , and  $\theta_B$  are amplitude and phase coefficients that depend on the input two-photon state and scattering matrix,  $\theta$  is the relative global phase between the active and reference SLM areas,  $k$  and  $l$  are two arbitrarily chosen output spatial modes with transverse positions  $(x_k, y_k)$  and  $(x_l, y_l)$  (see Method for details). In Equation (2), the  $2\theta$  oscillation arises from the two-photon paths linking one input to two outputs (Figs. 2a-b), while the  $\theta$  oscillation originates from paths linking two inputs to two outputs (Figs. 2c-d). Figure 2e shows an example of  $\Gamma_{kl}$  function of  $\theta$  measured experimentally using the setup described later in Figure 2f. The value of  $\theta$  maximizing  $\Gamma_{kl}$  is determined by phase-shifting digital holography or by fitting the data with equation 2 (see Methods), and is then applied to the pixels in the active area. The algorithm proceeds by selecting and shifting a

new subset of pixels at each step, repeating this process until the optimization target no longer evolves.

#### IV. EXPERIMENT

This algorithm is implemented using the experimental setup described in Figure 2.f. Pairs of photons at 810 nm with the same polarization are generated via type-I spontaneous parametric down-conversion (SPDC) in a thin  $\beta$ -barium borate (BBO) crystal illuminated by a collimated continuous-wave 405 nm laser. The resulting two-photon state is entangled in high spatial dimensions [28]. The crystal output surface is imaged onto an SLM using a  $4f$  telescope, which is itself imaged onto an optical plane near where a thing scattering medium (layer of parafilm) is placed. At the output, the photons are collected by a lens and a SPAD camera. The optical elements are arranged so that, without a medium, a Fourier plane of the crystal is imaged onto the SPAD, detecting photons in the momentum basis.

Figure 2g shows an optimization curve obtained by modulating the incident wavefront while monitoring a coincidence target over 200 steps. At the input, the SLM is divided into  $8 \times 8$  macro-pixels, each  $37 \times 37$  SLM pixels. At the output,  $\Gamma$  is measured and projected along the sum-coordinate axis to obtain  $\Gamma^+$ , which takes the form of an image, as seen previously in Figures 1f and g. The optimization target is the coincidence value at an arbitrary pixel  $T$  of  $\Gamma^+$ . From the SPAD camera perspective, the value  $\Gamma_T^+$  corresponds to the sum of coincidence rates between all symmetric pixel pairs around a pixel at position  $(x_T, y_T)$  i.e.  $\Gamma_T^+ = \sum_{k=1}^M \Gamma_{T+k, T-k}$ , where  $T-k$  (resp.  $T+k$ ) corresponds to a pixel at  $(x_T - x_k, y_T - y_k)$  (resp.  $(x_T + x_k, y_T + y_k)$ ), and  $M$  is the total number of pixels. In our experimental configuration, maximizing  $\Gamma_T^+$  is theoretically equivalent to optimizing  $\Gamma_{kl}$  for any pair of spatial modes  $k$  and  $l$ , with the practical advantage of yielding to stronger signal (see Methods).

At each optimization step, half of the macro-pixels are randomly chosen and shifted using 6 or 9 phase increments between 0 and  $2\pi$ , respectively for holography or fitting (see Methods). Values of  $\Gamma_T^+$  for different phases  $\theta$  are then fitted using the model in equation 2 to determine the optimal phase shift, which is then applied to the SLM active area. Each measurement takes about 5 minutes, totaling about 120 hours to reach the plateau. Figures 2h-j show the images  $\Gamma^+$  at various steps, illustrating the emergence of a peak at the target position, which confirms successful refocusing of photon-pair correlations after the scattering medium.

Ultimately, the optimization converges towards the phase mask shown in Figure 3a. The focusing peak shown in Figure 3b is approximately 5 times more intense than the average two-photon speckle surrounding it, while the direct intensity image remains homogeneous (inset). Interestingly, when replacing the photon pair source with a laser of the same polarization and frequency, we do not

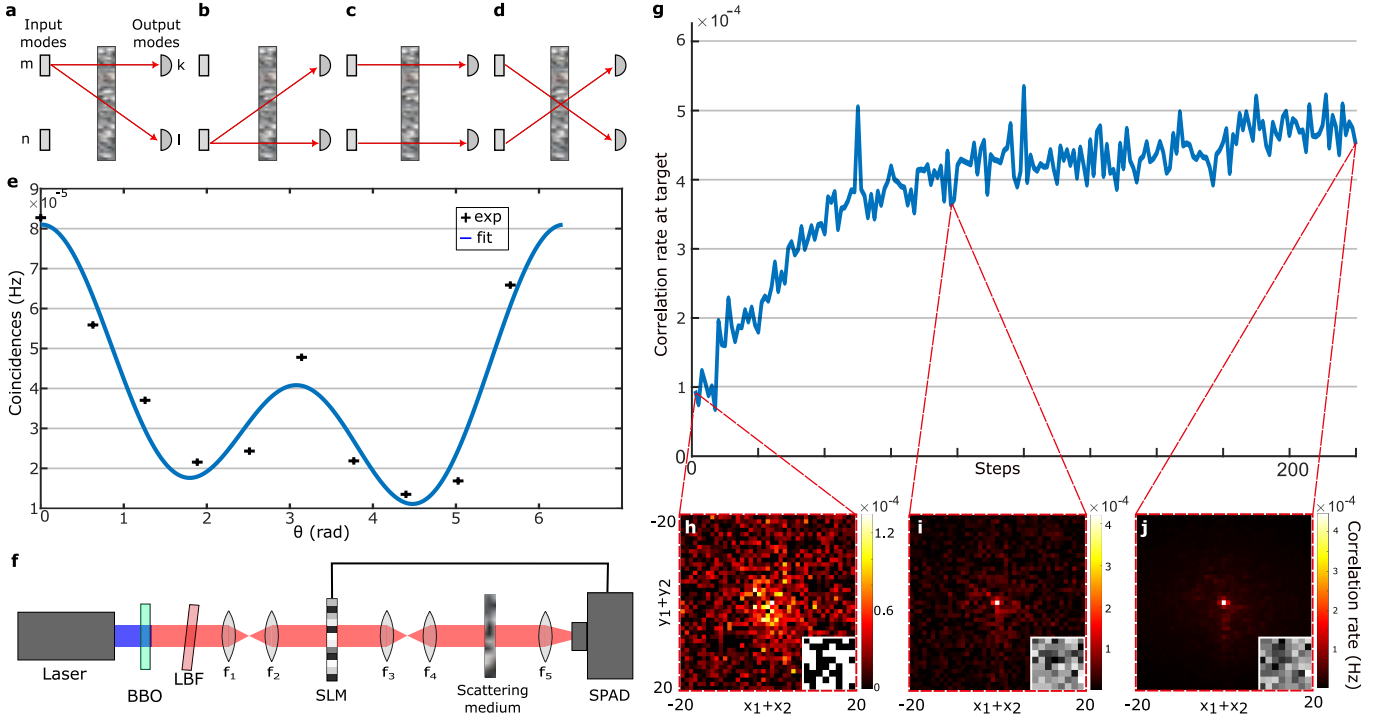


Figure 2. **Optimization process.** Four two-photon interference paths occur between two input modes (SLM pixels) and two output modes (SPAD pixels): **a and b**, Two photons originating from a single input mode  $m$  or  $n$  and detected at each output modes  $k$  and  $l$ . **c**, Two photons originating from two input modes  $m$  and  $n$  detected at output modes  $k$  and  $l$ , and **(d)** vice versa. **e**, Experimental measurement of  $\Gamma_{kl}$  between two arbitrary output modes  $k$  and  $l$  as a function of the phase  $\theta$  between the active and reference areas of the SLM. 10 points are measured (black crosses) and fitting the data (blue curve) enables to determine the coefficients  $A=2.21 \cdot 10^{-5}$  Hz,  $B=2.0 \cdot 10^{-5}$  Hz,  $C=3.87 \cdot 10^{-5}$  Hz,  $\theta_A=0.03$  rad,  $\theta_B=-0.14$  rad  $R^2 = 0.93$ ) and an optimal phase value of approximately 0.03 rad. **f**, A collimated diode laser (405 nm) illuminates  $\beta$ -barium borate (BBO) crystal with a thickness of 0.5mm to produce spatially entangled pairs of photons by type I spontaneous parametric down conversion (SPDC). A long-pass (LPF) positioned after the crystal remove pump photons. Lenses  $f_1 - f_2$  image the crystal surface onto a spatial light modulator (SLM), that is itself imaged by lenses  $f_3 - f_4$  onto an optical plane where a scattering medium is positioned. The distance between two successive lenses equals the sum of their focal lengths. At the output, a lens  $f_5$  and a single-photon avalanche diode (SPAD) camera positioned in its focal plane collect the photons. A band-pass filter  $810 \pm 5$ nm is positioned in front of the camera (not represented). **g**, Optimization curve showing the evolution of the correlation value at the target point as a function of the number of steps taken in the optimization procedure. The enhancement factor is approximately 5. **h-j**,  $\Gamma^+$  and SLM phase patterns (insets) at three different steps of the process. More details on the experimental setup can be found in supplementary section IV.

observe any refocusing of the classical light in the output intensity image in Figure 3c. Instead, a speckle pattern appears. This phase mask thus mitigates scattering for entangled photons, but not for classical light.

This result is surprising, in particular when it is compared to the outcome obtained using a classical optimization approach. In this case, the intensity at the center of the output camera is first maximized with the laser at the input using the method of Ref. [1], resulting in an intense peak visible in Figure 3f. Then, the classical source is replaced by photon pairs while maintaining the same phase mask on the SLM (Fig. 3d). A peak appears in the sum-coordinate projection in Figure 3e, with a value similar to that obtained using the non-classical optimization approach. Non-classical optimization thus converges to phase masks distinct from the classical solution, yet still refocuses entangled photons at the medium output. Ad-

ditional simulations shown in supplementary section VI and VIII confirm that these results are reproducible in a range of parameters, even for thicker scattering media (e.g. multiple layers of parafilm stacked together).

The existence of these ‘non-classical’ solutions i.e. phase masks that refocus entangled photons without refocusing classical light, is intrinsically linked to the presence of entanglement in the input state. Indeed, if we consider a two-photon state similar to that in our experiments, but with a wavefunction that is factorizable  $\psi_{nm}^{(i)} = E_n^{(i)} E_m^{(i)}$ , equation 1 simplifies to

$$\Gamma_{kl} = \left| E_k^{(o)} E_l^{(o)} \right|^2, \quad (3)$$

where  $E_k^{(o)} = \sum_n t_{kn} E_n^{(i)} e^{i\theta_n}$  is the optical field in output mode  $k$  obtained after propagation of a classical optical field  $E^{(i)}$  through the scattering medium. In this case,

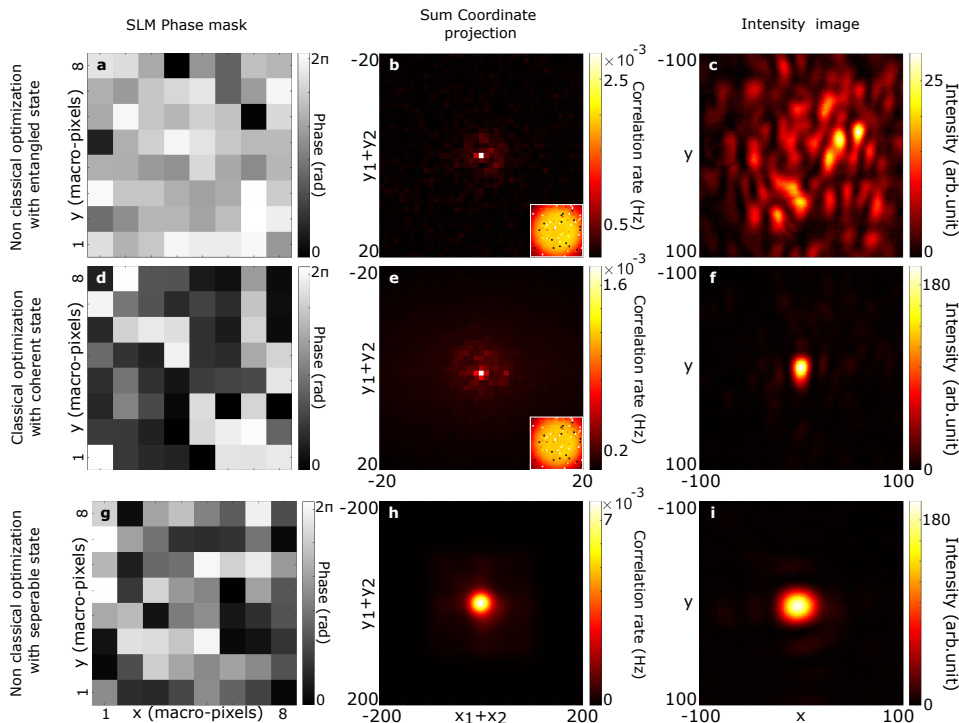


Figure 3. **Focusing results.** SLM phase mask (a) and sum-coordinate projection (b) obtained after refocusing spatial correlations using non-classical optimization with a two-photon entangled state at the input. The output intensity image is shown in inset. Speckle intensity (c) observed at the output after replacing the two-photon state with classical coherent light. SLM phase mask (d) obtained through classical optimization. In this case, classical light is first refocused in the output intensity (f). After replacing the classical source with entangled photon pairs, refocusing is then also observed in the sum-coordinate projection (e). The output intensity image is shown in the inset. SLM phase mask (g) and sum-coordinate projection (h) obtained after refocusing spatial correlations using non-classical optimization using a classical coherent state at the input to mimic a non-entangled two-photon state. After optimization, focusing is also observed in the intensity image (i)

maximizing correlations between output modes  $k$  and  $l$  is equivalent to maximizing the product of their respective intensities. Experimentally, this can be mimicked using classical light at the input and optimizing the product of output intensities. After such an optimization, a correlation peak is observed in the sum-coordinate projection shown in Figure 3h. Unlike the entangled case, however, a focus is also observed at the center of the output intensity image in Figure 3i. In this case therefore, the classical and non-classical optimization methods are equivalent. This result, along with additional experiments in supplementary section VI, confirms that optimizing spatial correlations of a non-entangled two-photon state consistently converges to the classical solution.

Note that the presence of entanglement is a necessary but not sufficient condition for reaching a non-classical solutions. Figures 4 compares non-classical solutions obtained with entangled two-photon input states of different Schmidt numbers  $K$  to the classical solution (that has  $K = 1$ ). As  $K$  decreases, deviating further from our experimental case  $K_{exp} = 1849$ , there is a threshold around  $K \approx 200$  beyond which all non-classical optimizations systematically converge to the classical solution.

## V. DISCUSSION

In this work, we implement a non-classical optimization approach using an entangled two-photon state propagating through a scattering medium, using as feedback for the SLM pattern the photon coincidence signal from a SPAD camera. We demonstrate the existence of specific ‘non-classical’ solutions that enable the refocusing of entangled photon pairs without refocusing classical light. In other words, the medium is rendered ‘transparent’ for photon pairs while remaining opaque to classical light. Remarkably, these solutions cannot be reached using classical optimization algorithms and have never been observed in previous studies.

In addition, we show that the existence of these non-classical solutions is directly linked to the presence of entanglement. To understand this, it is essential to recall a key property of an entangled state: the correlations it produces persist across multiple bases [34]. During optimization, the SLM and scattering medium - forming a linear optical system - reconfigure to implement a spatial basis transformation that maximizes correlations or intensity, without predefined constraints. Classically, only

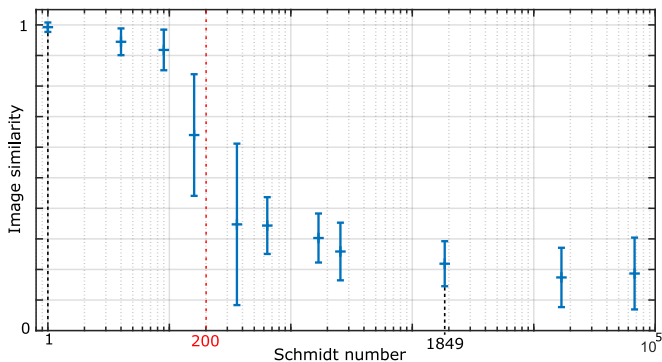


**Figure 4. Non-classical optimization and entanglement.** Results from simulations of non-classical optimization conducted with two-photon states of different Schmidt numbers, using an experimentally measured transmission matrix. The y-axis shows image similarity (calculated with `corr2` function in Matlab) between the classical intensity image obtained after each non-classical optimization using a state with Schmidt number  $K$  and that for a state  $K = 1$  (i.e. classical solution). The x-axis indicates the Schmidt number of the input state. For each Schmidt number, the optimization is repeated 5 times, and the error bars at each point represent the standard deviation of the obtained image similarity values. Schmidt numbers  $K_{exp} = 1849$  and  $K = 1$  correspond to the experimental cases studied in Figures 3a-c (high-dimensional entangled state) and Figures 3g-i (non-entangled state), respectively. The vertical dashed red line marks the threshold ( $K \approx 200$ ) below which non-classical optimization always converges to the classical solution. All images units are in pixels. All intensity and correlation images were acquired by replacing the SPAD camera with a CCD camera. See Methods for more details on the simulations.

a basis approximating the identity transformation works. For entangled states, however, multiple bases become accessible, allowing the system to converge toward one of them, which does not necessarily correspond to the identity. Interestingly, our non-local optimization implementation can also be used as an optical platform to simulate computationally hard problems. For example, by restricting the SLM pixel modulation to binary values (0 or  $\pi/2$ ), the system implements the energy function of an Ising model involving multi-spin interactions, described by the Hamiltonian:

$$H(\sigma) = -\frac{1}{2} \sum_{nm} J_{nm}^T \sigma_n \sigma_m - \frac{1}{2} \sum_{nml} \Lambda_{nml}^T \sigma_n \sigma_m \sigma_l - \frac{1}{2} \sum_{nmlp} Q_{nmlp}^T \sigma_n \sigma_m \sigma_l \sigma_p - \frac{1}{2} \sum_n K_n^T \sigma_n, \quad (4)$$

where  $\sigma_i = \{1, -1\}$ ,  $K_n^T$ ,  $J_{nm}^T$ ,  $\Lambda_{nml}^T$  and  $Q_{nmlp}^T$  depend on the transmission matrix coefficients, the input two-photon wavefunction, the SLM macropixel size and the optimization target  $T$  (see Methods and Supplementary Section X). Optimizing a target coincidence rate at the output corresponds to minimizing  $H$  to determine the ground state, as experimentally demonstrated

in Figure 5a. After non-classical optimization, the sum-coordinate projection show a focus at the target position (Fig. 5b) and the SLM phase has converged to a state corresponding to a local minimum of the energy (Fig. 5c). Such complex Hamiltonians with both three-spin ( $\sigma_i \sigma_j \sigma_k$ ) and four-spin ( $\sigma_i \sigma_j \sigma_k \sigma_l$ ) interactions cannot be simulated with similar optical Ising machines operated with classical light [6, 35]. These could help solve novel computationally hard problems, such as interpreting supercooled liquid behavior [36].

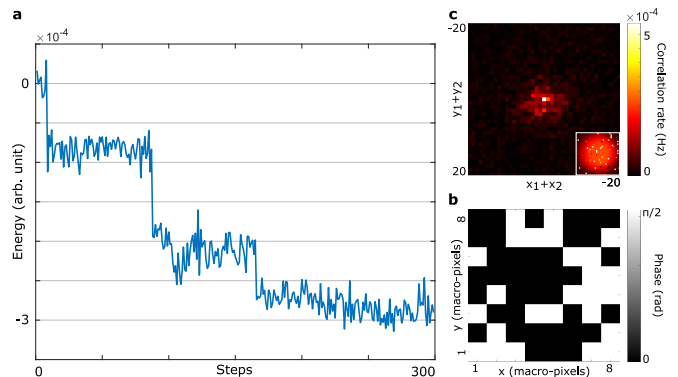


**Figure 5. Optical simulation of an Ising model with multi-spin interactions.** **a**, Energy of the Ising model as the number of optimization steps. The optimization is performed with  $8 \times 8$  SLM macropixels at the input, each taking only two values, 0 or  $\pi/2$ . **b**, Sum-coordinate projection  $\Gamma^+$  measured at the end of the optimization, in which the central target pixel rises above the background. **c**, Optimal SLM phase mask reached after 300 steps of optimization (100 hours), corresponding to the ground state of the simulated system. The spins up (+1) and down (-1) correspond to the values of 0 and  $\pi/2$ , respectively.

Beyond optical simulators, non-classical optimization is primarily a tool that helps mitigate external disturbances to a quantum state, a major challenge in quantum technologies. In optics, this issue arises in various practical scenarios, such as quantum imaging systems affected by optical aberrations [17, 37], quantum communication through turbulent atmospheres and fibers [18, 23, 38], and even quantum computation algorithms where error correction is needed [39]. In this context, our study demonstrates that quantum entanglement could play a key role, as in our case its presence preserves the quantum state integrity through the random medium, while classical light remains scattered.

## METHODS

**Details on Equation (1).** Considering photons degenerate in frequency and polarization, a pure two-photon state at the input ( $i$ ) or output ( $o$ ) is expressed as

$$|\Psi^{(i/o)}\rangle = \iint \psi^{(i/o)}(\mathbf{r}_1, \mathbf{r}_2) a_{\mathbf{r}_1}^\dagger a_{\mathbf{r}_2}^\dagger d\mathbf{r}_1 d\mathbf{r}_2 |0\rangle, \quad (5)$$

where  $a_{\mathbf{r}_1}^\dagger$  is the photon creation operator in the spatial mode  $\mathbf{r}_1$ , and  $\psi^{(i/o)}(\mathbf{r}_1, \mathbf{r}_2)$  represents the spatial two-photon wavefunction at the input or output. Additionally, the scattering medium is linear and can be described, in a discretized space, by a transmission matrix  $t_{kl}$ , where  $l$  represents, for instance, an SLM pixel at the input and  $k$  represents a camera pixel at the output. By evolving each creation operator as

$$a_k^\dagger \rightarrow \sum_l t_{kl} a_l^\dagger, \quad (6)$$

one can derive Equation (1), which relates the discrete two-photon wavefunctions  $\psi^{(o)}$  and  $\psi^{(i)}$ .

**Details on Equation (2).** Considering two output modes  $k$  and  $l$  and two SLM areas, denoted  $\mathcal{M}$  and  $\mathcal{N}$  (active and reference areas), the coincidence rate  $\Gamma_{kl}$  results from the coherent sum of complex terms associated with the two-photon interference processes shown in Figure 2a-d.

$$\Gamma_{kl} = \left| e^{2i\theta_{\mathcal{M}}} S_{\mathcal{M}} + e^{2i\theta_{\mathcal{N}}} S_{\mathcal{N}} + e^{i(\theta_{\mathcal{M}} + \theta_{\mathcal{N}})} S_{\mathcal{M}, \mathcal{N}} \right|^2, \quad (7)$$

where  $\theta_{\mathcal{M}}$  and  $\theta_{\mathcal{N}}$  are the phases of the active and reference areas and

$$S_{\mathcal{M}} = \sum_{m \in \mathcal{M}} t_{km} t_{lm} \psi_{mm}^{(i)}, \quad (8)$$

$$S_{\mathcal{N}} = \sum_{n \in \mathcal{N}} t_{kn} t_{ln} \psi_{nn}^{(i)}, \quad (9)$$

$$S_{\mathcal{M}, \mathcal{N}} = \sum_{m \in \mathcal{M}, n \in \mathcal{N}} [t_{kn} t_{lm} + t_{km} t_{ln}] \psi_{mn}^{(i)}. \quad (10)$$

Expanding Equation (7) leads to:

$$\begin{aligned} \Gamma_{kl} &= |S_{\mathcal{M}}|^2 + |S_{\mathcal{N}}|^2 + |S_{\mathcal{M}, \mathcal{N}}|^2 \\ &+ e^{2i(\theta_{\mathcal{M}} - \theta_{\mathcal{N}})} S_{\mathcal{M}} S_{\mathcal{N}}^* + e^{-2i(\theta_{\mathcal{M}} - \theta_{\mathcal{N}})} S_{\mathcal{M}}^* S_{\mathcal{N}} \\ &+ e^{i(\theta_{\mathcal{M}} - \theta_{\mathcal{N}})} S_{\mathcal{M}} S_{\mathcal{M}, \mathcal{N}}^* + e^{-i(\theta_{\mathcal{M}} - \theta_{\mathcal{N}})} S_{\mathcal{M}}^* S_{\mathcal{M}, \mathcal{N}} \\ &+ e^{i(\theta_{\mathcal{N}} - \theta_{\mathcal{M}})} S_{\mathcal{N}} S_{\mathcal{M}, \mathcal{N}}^* + e^{-i(\theta_{\mathcal{N}} - \theta_{\mathcal{M}})} S_{\mathcal{N}}^* S_{\mathcal{M}, \mathcal{N}}. \end{aligned} \quad (11)$$

By identifying the coefficients of Equation (11) with those of Equation (2), we find:

$$\theta = \theta_{\mathcal{M}} - \theta_{\mathcal{N}} \quad (12)$$

$$A = 2|S_{\mathcal{M}} S_{\mathcal{N}}^*| \quad (13)$$

$$\theta_A = \arg(S_{\mathcal{M}} S_{\mathcal{N}}^*) \quad (14)$$

$$B = 2|S_{\mathcal{M}} S_{\mathcal{M}, \mathcal{N}}^* + S_{\mathcal{N}} S_{\mathcal{M}, \mathcal{N}}^*| \quad (15)$$

$$\theta_B = \arg(S_{\mathcal{M}} S_{\mathcal{M}, \mathcal{N}}^* + S_{\mathcal{N}} S_{\mathcal{M}, \mathcal{N}}^*) \quad (16)$$

$$C = |S_{\mathcal{M}}|^2 + |S_{\mathcal{N}}|^2 + |S_{\mathcal{M}, \mathcal{N}}|^2. \quad (17)$$

**Determination of the optimal phase.** Determining the value of  $\theta$  that maximizes  $\Gamma$  at each optimization step is done in two stages. First, the coefficients  $A$ ,  $B$ ,

$C$ ,  $\theta_A$ , and  $\theta_B$  are determined by measuring  $\Gamma$  for six phase values  $\{0, \pi/4, \pi/2, \pi, 3\pi/2, 5\pi/4\}$  as follows:

$$B e^{i\theta_B} = \frac{\Gamma(0) - \Gamma(\pi)}{2} + i \frac{\Gamma(3\pi/2) - \Gamma(\pi/2)}{2} \quad (18)$$

$$C = \frac{\Gamma(0) + \Gamma(\pi) + \Gamma(3\pi/2) + \Gamma(\pi/2)}{4} \quad (19)$$

$$A e^{i\theta_A} = \frac{\Gamma(0) + \Gamma(\pi) - 2C}{2} + i \frac{\Gamma(\pi/4) + \Gamma(5\pi/4) - 2C}{2} \quad (20)$$

To reduce uncertainty due to measurement noise, one can also measure more than six points and fit them to the model of Equation (2) by minimizing the sum of squared errors. Once the coefficients are known, the optimal value of  $\theta$  is determined analytically by solving a fourth-degree polynomial equation or using a numerical approach. More details can be found in supplementary section III.

**Measurement of  $\Gamma$  and sum-coordinate projection.** The spatially resolved second-order correlation function  $\Gamma_{kl}$ , where  $k$  and  $l$  are two pixels of the SPAD camera centred at transverse positions  $(x_k, y_k)$  and  $(x_l, y_l)$ , is measured by acquiring a set of  $P + 1$  frames  $\{I^{(p)}\}_{p \in \llbracket 1, P+1 \rrbracket}$  using a fixed exposure time and processing them using the formula [31, 40]:

$$\Gamma_{kl} = \frac{1}{P} \sum_{p=1}^P [I_k^{(p)} I_l^{(p)} - I_k^{(p)} I_l^{(p+1)}]. \quad (21)$$

Because the SPAD camera does not resolve the number of photons, photon coincidences at the same pixel (i.e. coefficients  $\Gamma_{kk}$ ) cannot be measured, and are therefore set to zero. In addition, correlation values between neighboring pixels suffer from cross-talk and must be corrected, as detailed in Ref. [21]. The sum-coordinate projection of  $\Gamma$  is then calculated using the following formula:

$$\Gamma_T^+ = \sum_{k=1}^M \Gamma_{T-k, T+k}, \quad (22)$$

where  $T+k$  (resp.  $T-k$ ) denotes camera pixels of transverse position  $(x_T + x_k, y_T + y_k)$  (resp.  $(x_T - x_k, y_T - y_k)$ ).

**Optimization target.** In our experiments, we opted to use  $\Gamma_T^+$  as an optimization target instead of directly  $\Gamma_{kl}$ . The reason is practical. Indeed, when the scattering medium is sufficiently thin, it can be shown that  $\Gamma_T^+$  simplifies as follows:

$$\Gamma_T^+ \approx M |\psi_{T+k, T-k}^{(o)}|^2, \quad (23)$$

where  $k$  denotes any camera pixel. Equation (23) shows that optimizing an arbitrary position  $t$  in the sum-coordinate projection of  $\Gamma$  is equivalent to optimizing the coincidences between any pair of arbitrarily chosen pixels on the camera, thus bringing us back to the general problem posed in equation 1. More importantly,

in this case, the coincidence rate at the target output is amplified by a factor  $M \sim 1000$ , drastically reducing acquisition times. This choice of target and experimental configuration makes the experiment feasible with current detection technologies while keeping the general applicability of our approach. See Supplementary Section V for a demonstration of Equation (23). Note that Equation (23) is not a prerequisite for non-classical optimization. In thicker scattering media, it does not hold, yet simulations (Supplementary Section VI) show the non-classical optimization still works. However, the low signal-to-noise (i.e. absence of the amplification factor  $M$ ) makes the experimental implementation challenging.

**Details on the simulations.** The simulations shown in Figure 5 were performed by propagating the two-photon state through the optical system using matrix multiplication in Matlab. The scattering matrices used, of size  $M \times N$ , were measured experimentally following the method described in Ref. [26]. The input state incident on the SLM is modeled using a Double-Gaussian model [41], fully characterized by its momentum correlation width  $\sigma_{\mathbf{k}} \approx 8.0 \cdot 10^2 m^{-1}$  and the position correlation width  $\sigma_{\mathbf{r}} \approx 2.9 \cdot 10^{-5} m$ . These values are experimentally determined by imaging the SLM onto an Electron Multiplied Charge Couple Device (EMCCD) camera, as explained in supplementary Document Section VII. Before propagation, the state is discretized into input modes, i.e. the macropixels of the SLM, taking into account their size and number. To produce Figure 5.g, simulations were conducted by varying  $\sigma_{\mathbf{r}}$  from 0 to 260, while  $\sigma_{\mathbf{k}}$  was fixed. The Schmidt number  $K$  is then calculated using the equation  $K = 1/(\sigma_{\mathbf{k}}\sigma_{\mathbf{r}})^2$  [41]. Further details on the simulations are provided in Supplementary Section VIII.

**Details on Equation (4).** Equation (4) is de-

rived by expanding Equation (1) under the following assumptions: (i) The input two-photon wavefunction is approximated as  $\psi_{mn}^{(i)} \approx \delta_{m-n} + \alpha\delta_{m-n+1}$ , where  $\delta$  is the Dirac delta function,  $m$  represents a spatial input mode corresponding to an SLM macropixel centered at the transverse position  $(x_m, y_m)$ , and  $\alpha$  is a parameter dependent on both the state characteristics and the SLM macropixel size (see Supplementary Section VII). This approximation holds in our experimental configuration, with  $\alpha \approx 0.1$  measured experimentally. (ii) The phase encoded at an arbitrary input mode  $n$  takes values 0 or  $\pi/2$ , with the corresponding field given by  $\epsilon_n = \{1, i\}$ . Under this encoding, the relations  $\sigma_n = \epsilon_n^2$  and  $\epsilon_n\epsilon_m = \frac{1}{2}(\sigma_n + \sigma_m) + \frac{i}{2}(1 - \sigma_n\sigma_m)$  are used to simplify Equation (1). Further details, including the full expressions for the parameters  $K_n^T$ ,  $J_{nm}^T$ ,  $\lambda_{nml}^T$ , and  $Q_{nmlp}^T$ , can be found in Supplementary Section X.

**Energy minimization.** The minimized energy in Figure 5 is defined as the negative of the target coincidence rate in the output sum-coordinate projection. To reduce it, each optimization step randomly selects 25% of the  $8 \times 8$  spatial input modes (SLM macropixels) and limits the phase encoding to 0 or  $\pi/2$ , effectively flipping the spins i.e. all values at 0 are set to  $\pi/2$  and vice versa. After flipping, the energy is evaluated, and the new configuration is kept only if the energy decreases. In our experiment, flipping 25% of the spins ensures a sufficient signal-to-noise ratio for each measurement, though in theory, spins could be flipped individually. This fraction also determines the accuracy of the ground state found with the method, and explains the plateaus observed in the minimization curve in Figure 5a. In this experiment, the scattering medium was created by programming a fixed random phase pattern on the SLM, with similar complexity than the layer of parafilm used in the other experiments. More details are provided in Supplementary Section X.

- 
- [1] I. M. Vellekoop and A. P. Mosk, Focusing coherent light through opaque strongly scattering media, *Optics Letters* **32**, 2309 (2007).
- [2] R. Horstmeyer, H. Ruan, and C. Yang, Guidestar-assisted wavefront-shaping methods for focusing light into biological tissue, *Nature photonics* **9**, 563 (2015).
- [3] S. Gigan, O. Katz, H. B. d. Aguiar, E. R. Andresen, A. Aubry, J. Bertolotti, E. Bossy, D. Bouchet, J. Brake, S. Brasselet, Y. Bromberg, H. Cao, T. Chaigne, Z. Cheng, W. Choi, T. Čížmár, M. Cui, V. R. Curtis, H. Defienne, M. Hofer, R. Horisaki, R. Horstmeyer, N. Ji, A. K. LaViolette, J. Mertz, C. Moser, A. P. Mosk, N. C. Pégard, R. Piestun, S. Popoff, D. B. Phillips, D. Psaltis, B. Rahmani, H. Rigneault, S. Rotter, L. Tian, I. M. Vellekoop, L. Waller, L. Wang, T. Weber, S. Xiao, C. Xu, A. Yamilov, C. Yang, and H. Yilmaz, Roadmap on wavefront shaping and deep imaging in complex media, *Journal of Physics: Photonics* **4**, 042501 (2022), publisher: IOP Publishing.
- [4] T. Čížmár and K. Dholakia, Shaping the light transmission through a multimode optical fibre: complex transformation analysis and applications in biophotonics, *Optics express* **19**, 18871 (2011).
- [5] M. A. Taylor, M. Waleed, A. B. Stilgoe, H. Rubinsztein-Dunlop, and W. P. Bowen, Enhanced optical trapping via structured scattering, *Nature Photonics* **9**, 669 (2015).
- [6] D. Pierangeli, M. Rafayelyan, C. Conti, and S. Gigan, Scalable spin-glass optical simulator, *Physical Review Applied* **15**, 034087 (2021).
- [7] M. Leonetti, E. Hörmann, L. Leuzzi, G. Parisi, and G. Ruocco, Optical computation of a spin glass dynamics with tunable complexity, *Proceedings of the National Academy of Sciences* **118**, e2015207118 (2021).
- [8] O. Lib and Y. Bromberg, Quantum light in complex media and its applications, *Nature Physics* **18**, 986 (2022).

- [9] T. J. Huisman, S. R. Huisman, A. P. Mosk, and P. W. H. Pinkse, Controlling single-photon Fock-state propagation through opaque scattering media, *Applied Physics B* **116**, 603 (2014).
- [10] H. Defienne, M. Barbieri, B. Chalopin, B. Chatel, I. A. Walmsley, B. J. Smith, and S. Gigan, Nonclassical light manipulation in a multiple-scattering medium, *Optics Letters* **39**, 6090 (2014), publisher: Optica Publishing Group.
- [11] T. A. W. Wolterink, R. Uppu, G. Ctistis, W. L. Vos, K.-J. Boller, and P. W. H. Pinkse, Programmable two-photon quantum interference in  $\{10\}^{\{3\}}$  channels in opaque scattering media, *Physical Review A* **93**, 053817 (2016), publisher: American Physical Society.
- [12] J. Carpenter, B. J. Eggleton, and J. Schröder, 110x110 optical mode transfer matrix inversion, *Optics Express* **22**, 96 (2014), publisher: Optica Publishing Group.
- [13] H. Defienne, M. Barbieri, I. A. Walmsley, B. J. Smith, and S. Gigan, Two-photon quantum walk in a multimode fiber, *Science Advances* **2**, e1501054 (2016), publisher: American Association for the Advancement of Science.
- [14] S. Leedumrongwatthanakun, L. Innocenti, H. Defienne, T. Juffmann, A. Ferraro, M. Paternostro, and S. Gigan, Programmable linear quantum networks with a multimode fibre, *Nature Photonics* **14**, 139 (2020), publisher: Nature Publishing Group.
- [15] S. Goel, S. Leedumrongwatthanakun, N. H. Valencia, W. McCutcheon, A. Tavakoli, C. Conti, P. W. H. Pinkse, and M. Malik, Inverse design of high-dimensional quantum optical circuits in a complex medium, *Nature Physics*, 1 (2024), publisher: Nature Publishing Group.
- [16] A. Makowski, M. Dąbrowski, I. M. Antolovic, C. Bruschini, H. Defienne, E. Charbon, R. Lapkiewicz, and S. Gigan, Large reconfigurable quantum circuits with SPAD arrays and multimode fibers, *Optica* **11**, 340 (2024), publisher: Optica Publishing Group.
- [17] P. Cameron, B. Courme, C. Vernière, R. Pandya, D. Faccio, and H. Defienne, Adaptive optical imaging with entangled photons, *Science* **383**, 1142 (2024).
- [18] N. H. Valencia, S. Goel, W. McCutcheon, H. Defienne, and M. Malik, Unscrambling entanglement through a complex medium, *Nature Physics* **16**, 1112 (2020), number: 11 Publisher: Nature Publishing Group.
- [19] O. Lib, G. Hasson, and Y. Bromberg, Real-time shaping of entangled photons by classical control and feedback, *Science Advances* **6**, eabb6298 (2020), publisher: American Association for the Advancement of Science.
- [20] F. Devaux, A. Mosset, S. M. Popoff, and E. Lantz, Restoring and tailoring very high dimensional spatial entanglement of a biphoton state transmitted through a scattering medium, *Journal of Optics* **25**, 055201 (2023), publisher: IOP Publishing.
- [21] B. Courme, P. Cameron, D. Faccio, S. Gigan, and H. Defienne, Manipulation and Certification of High-Dimensional Entanglement through a Scattering Medium, *PRX Quantum* **4**, 010308 (2023), publisher: American Physical Society.
- [22] R. Shekel, O. Lib, and Y. Bromberg, Shaping entangled photons through arbitrary scattering media using an advanced wave beacon, *Optica Quantum* **2**, 303 (2024).
- [23] M. T. Gruneisen, M. L. Eickhoff, S. C. Newey, K. E. Stoltenberg, J. F. Morris, M. Bareian, M. A. Harris, D. W. Oesch, M. D. Oliker, M. B. Flanagan, et al., Adaptive-optics-enabled quantum communication: A technique for daytime space-to-earth links, *Physical Review Applied* **16**, 014067 (2021).
- [24] J. Zhao, Y. Zhou, B. Braverman, C. Liu, K. Pang, N. K. Steinhoff, G. A. Tyler, A. E. Willner, and R. W. Boyd, Performance of real-time adaptive optics compensation in a turbulent channel with high-dimensional spatial-mode encoding, *Optics express* **28**, 15376 (2020).
- [25] L. Scarfe, F. Hufnagel, M. F. Ferrer-Garcia, A. D'Errico, K. Heshami, and E. Karimi, Fast Adaptive Optics for High-Dimensional Quantum Communications in Turbulent Channels (2023), arXiv:2311.13041 [physics, physics:quant-ph].
- [26] S. M. Popoff, G. Lerosey, R. Carminati, M. Fink, A. C. Boccara, and S. Gigan, Measuring the Transmission Matrix in Optics: An Approach to the Study and Control of Light Propagation in Disordered Media, *Physical Review Letters* **104**, 100601 (2010).
- [27] C. Stockbridge, Y. Lu, J. Moore, S. Hoffman, R. Paxman, K. Toussaint, and T. Bifano, Focusing through dynamic scattering media, *Optics express* **20**, 15086 (2012).
- [28] S. P. Walborn, C. Monken, S. Pádua, and P. S. Ribeiro, Spatial correlations in parametric down-conversion, *Physics Reports* **495**, 87 (2010).
- [29] H. Defienne, M. Reichert, and J. W. Fleischer, Adaptive Quantum Optics with Spatially Entangled Photon Pairs, *Physical Review Letters* **121**, 233601 (2018), publisher: American Physical Society.
- [30] J. R. Ott, N. A. Mortensen, and P. Lodahl, Quantum interference and entanglement induced by multiple scattering of light, *Physical review letters* **105**, 090501 (2010).
- [31] B. Ndagano, H. Defienne, A. Lyons, I. Starshynov, F. Villa, S. Tisa, and D. Faccio, Imaging and certifying high-dimensional entanglement with a single-photon avalanche diode camera, *npj Quantum Information* **6**, 1 (2020), number: 1 Publisher: Nature Publishing Group.
- [32] W. Peeters, J. Moerman, and M. Van Exter, Observation of two-photon speckle patterns, *Physical review letters* **104**, 173601 (2010).
- [33] I. M. Vellekoop and A. Mosk, Phase control algorithms for focusing light through turbid media, *Optics communications* **281**, 3071 (2008).
- [34] C. Spengler, M. Huber, S. Brierley, T. Adaktylos, and B. C. Hiesmayr, Entanglement detection via mutually unbiased bases, *Physical Review A—Atomic, Molecular, and Optical Physics* **86**, 022311 (2012).
- [35] D. Pierangeli, G. Marcucci, and C. Conti, Large-scale photonic ising machine by spatial light modulation, *Physical review letters* **122**, 213902 (2019).
- [36] D. Kivelson, S. A. Kivelson, X. Zhao, Z. Nussinov, and G. Tarjus, A thermodynamic theory of supercooled liquids, *Physica A: Statistical Mechanics and its Applications* **219**, 27 (1995).
- [37] B. Freitas, Y. Zhang, D. England, J. Lundeen, and B. Sussman, Quantum correlated image recording through noisy and turbulent channels, *ArXiv 10.1364/opticaopen.26973418.v1* (2024).
- [38] V. M. Acosta, D. Dequal, M. Schiavon, A. Montmerle-Bonnefois, C. B. Lim, J.-M. Conan, and E. Diamanti, Analysis of satellite-to-ground quantum key distribution with adaptive optics, *New Journal of Physics* **26**, 023039 (2024).
- [39] M. Müller, A. Rivas, E. Martínez, D. Nigg, P. Schindler, T. Monz, R. Blatt, and M. Martin-Delgado, Iterative phase optimization of elementary quantum error correct-

- ing codes, *Physical Review X* **6**, 031030 (2016).
- [40] H. Defienne, M. Reichert, and J. W. Fleischer, General Model of Photon-Pair Detection with an Image Sensor, *Physical Review Letters* **120**, 203604 (2018).
- [41] M. V. Fedorov, Y. M. Mikhailova, and P. A. Volkov, Gaussian modelling and Schmidt modes of SPDC biphoton states, *Journal of Physics B: Atomic, Molecular and Optical Physics* **42**, 175503 (2009).
- [42] J. Schneeloch and J. C. Howell, Introduction to the Transverse Spatial Correlations in Spontaneous Parametric Down-Conversion through the Biphoton Birth Zone, *Journal of Optics* **18**, 053501 (2016), arXiv:1502.06996 [quant-ph].
- [43] P.-A. Moreau, J. Mougins-Sisini, F. Devaux, and E. Lantz, Realization of the purely spatial Einstein-Podolsky-Rosen paradox in full-field images of spontaneous parametric down-conversion, *Physical Review A* **86**, 010101 (2012), publisher: American Physical Society.
- [44] M. P. Edgar, D. S. Tasca, F. Izdebski, R. E. Warburton, J. Leach, M. Agnew, G. S. Buller, R. W. Boyd, and M. J. Padgett, Imaging high-dimensional spatial entanglement with a camera, *Nature Communications* **3**, 984 (2012), number: 1 Publisher: Nature Publishing Group.

## Supplementary Materials: Non-classical optimization through complex media

Baptiste Courme<sup>1,2</sup>, Chloé Vernière<sup>1</sup>, Malo Joly<sup>2</sup>, Daniele Faccio<sup>3</sup>, Sylvain Gigan<sup>2</sup>, Hugo Defienne<sup>1</sup>

<sup>1</sup>*Sorbonne Université, CNRS, Institut des NanoSciences de Paris, INSP, F-75005 Paris, France*

<sup>2</sup>*Laboratoire Kastler Brossel, ENS-Université PSL, CNRS, Sorbonne Université, Collège de France, 24 rue Lhomond, 75005 Paris, France*

<sup>3</sup>*School of Physics and Astronomy, University of Glasgow, Glasgow G12 8QQ, UK*

### I. CLASSICAL OPTIMIZATION

In this section, we investigate the solutions that optimize the output intensity at a given spatial mode when a classical coherent state of light is shaped at the input of the scattering medium.

#### A. Demonstration

Focusing classical coherent light through a scattering medium by iterative optimization is described in Ref. [1]. In this case, one can show that the optimal solution is unique and that there are no local maxima. To demonstrate this, let us consider the matrix equation describing the propagation of classical coherent light through a scattering medium:

$$E^{(o)} = TE^{(i)}, \quad (\text{B1})$$

where  $T$  is the scattering matrix of the medium,  $E^{(o)}$  is a vector representing the output field discretized over the output spatial modes, and  $E^{(i)}$  is a vector representing the input field discretized over the input spatial modes. The intensity at an arbitrary output mode  $k$  is given by

$$I_k^{(o)} = \left| \sum_{l=1}^N E_l t_{kl} e^{i(\phi_{kl} + \alpha_l + \theta_l)} \right|^2, \quad (\text{B2})$$

where  $t_{kl} e^{i\phi_{kl}}$  is the matrix coefficient linking input mode  $l$  to output mode  $k$ ,  $E_l e^{i\alpha_l}$  is the field incident on mode  $l$  of the spatial light modulator (SLM),  $\theta_l$  is the phase implemented by the SLM at input mode  $l$ , and  $N$  is the total number of input modes. To simplify calculations without loss of generality, we redefine the quantities in Eq. (B2) as follows:  $|E_l t_{kl}| \rightarrow a_l$  and  $\phi_{kl} + \alpha_l + \theta_l \rightarrow \theta_l$ . In the following, we study the critical points of  $I^{(o)}$  as a function of the variables  $\{\theta_l\}_{l \in [1, N]}$ . By definition, critical points are found by setting the gradient to zero:

$$\forall l \in [1, N], \quad \frac{\partial I^{(o)}}{\partial \theta_l} = 0. \quad (\text{B3})$$

Expanding Equation (B3), we obtain another set of equations:

$$\forall l \in [1, N], \quad \sum_{p \neq l} a_l a_p \sin(\theta_l - \theta_p) = 0. \quad (\text{B4})$$

To solve Equation (B4), we combine the different equations and show that it is necessary for each term to cancel individually i.e.  $\forall (l, p) \in [1, N]^2, \sin(\theta_l - \theta_p) = 0$ . If we fix  $\theta_N = 0$  as the reference phase, the critical points of  $I^{(o)}$  are thus given by:

$$(\theta_1, \theta_2, \dots, \theta_{N-1}, \theta_N) = (0 \pm \pi, 0 \pm \pi, \dots, 0 \pm \pi, 0). \quad (\text{B5})$$

By analyzing the variations of  $I^{(o)}$  around these critical points, we find that only one critical point is a maximum:

$$(\theta_1, \theta_2, \dots, \theta_{N-1}, \theta_N) = (0, 0, \dots, 0, 0). \quad (\text{B6})$$

By performing the inverse change of variables  $\theta_l \rightarrow \phi_{kl} + \alpha_l + \theta_l$ , we have:

$$(\theta_1, \theta_2, \dots, \theta_{N-1}, \theta_N) = (-\phi_{k1} - \alpha_1, -\phi_{k2} - \alpha_2, \dots, -\phi_{kN-1} - \alpha_{N-1}, -\phi_{kN} - \alpha_N). \quad (\text{B7})$$

All other critical points correspond to either minima or saddle points. Hence, there is a unique maximum, which is necessarily the global maximum.

## B. Simulations

To illustrate this, let us consider a simple situation described in Figure S1a. At the input, we consider three spatial modes whose phases  $\theta_1$ ,  $\theta_2$ , and  $\theta_3$  can be independently adjusted. At the output, the intensity is measured at a single spatial mode. The parameter space has an effective dimension of 2, as the phases are defined up to a global constant i.e.  $\theta_1 + \theta_2 + \theta_3 = \text{constant}$ .

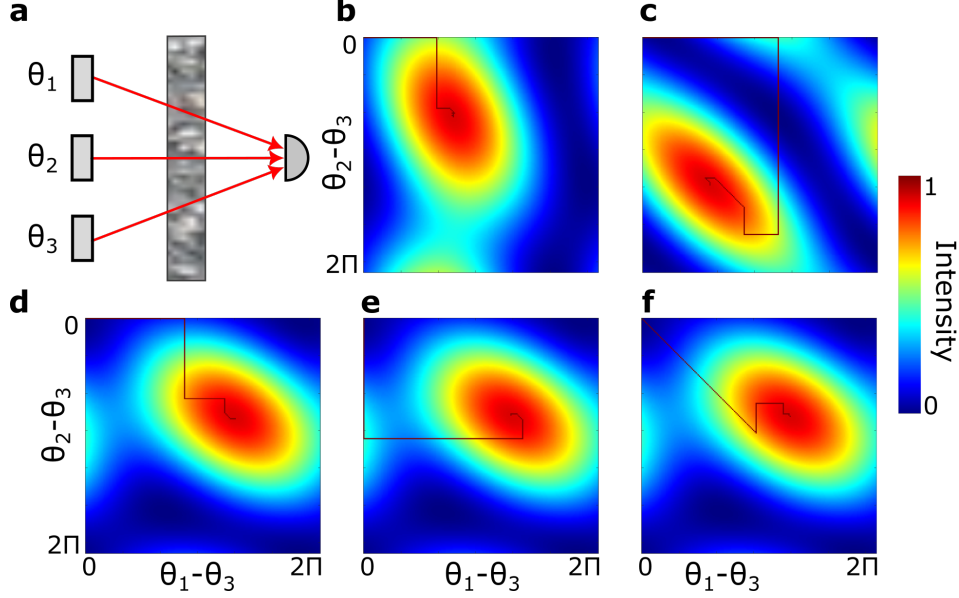


Figure S1. **Simulations of classical optimization with three input modes.** **a**, Classical coherent light propagates through a scattering medium. Three input spatial modes with controllable phases  $\theta_1$ ,  $\theta_2$ , and  $\theta_3$ , and one output spatial mode where the intensity is measured, are considered. The transmission matrix  $T$  is a  $1 \times 3$  matrix composed of random complex coefficients generated as  $T = \text{rand}(1, 3) \cdot \exp(i \cdot \text{rand}(1, 3) \cdot 2\pi)$ , where  $\text{rand}$  is a MATLAB function. **b-d**, Intensity values  $I^{(o)}(\theta_1, \theta_2)$  calculated for three different scattering matrices. The red line corresponds to the iterative optimization path in the parameter space using a partitioning algorithm. **d-f**, Three distinct iterative optimizations performed for the same scattering matrix, all converging towards the same unique maximum. In each optimization simulation, white noise with a variance of approximately 1% of the mean intensity was added to mimic experimental noise.

Figures S1.b-d show the intensity values at the output mode as a function of the parameters  $\theta_1 - \theta_3$  and  $\theta_2 - \theta_3$  for different scattering matrices. The scattering matrices  $T$  are composed of  $1 \times 3$  random complex coefficients. In the simulation, the output intensity value  $I^{(o)}(\theta_1, \theta_2)$  for the given phase values  $\theta_1$  and  $\theta_2$  is obtained by matrix multiplication:

$$I^{(o)}(\theta_1, \theta_2) = \left| T \begin{bmatrix} e^{i\theta_1} \\ e^{i\theta_2} \\ 1 \end{bmatrix} \right|^2. \quad (\text{B8})$$

Here, we calculate  $I^{(o)}(\theta_1, \theta_2)$  for 1000 values of  $\theta_1$  and  $\theta_2$ , each ranging from 0 to  $2\pi$ . The red line in each figure shows the path taken by the iterative optimization process. A partitioning algorithm is used to perform the optimization. At each step,  $\theta_1$ ,  $\theta_2$ , or  $\theta_3$  are randomly selected and scanned over the range 0 to  $2\pi$ . The phase value that maximizes the output intensity is then fixed before proceeding to the next step. We observe that there are no local maxima and that the algorithm always converges to the unique optimal solution. In addition, Figures S1.d-f show three different optimization process performed for the same scattering matrix. While the optimization paths are different, we observe that they all converge to the global maximum.

### C. Influence of the input field

Here, the shape of the input field to the SLM does not affect the optimization problem: there will still be a unique maximum and no local maxima. Indeed, if we consider an arbitrary input field denoted as

$$E^{(i)} = \begin{bmatrix} E_1^{(i)} \\ E_2^{(i)} \\ E_3^{(i)} \end{bmatrix},$$

the propagation equation can always be rewritten as:

$$I^{(o)}(\theta_1, \theta_2) = \left| T \begin{bmatrix} e^{i\theta_1} & 0 & 0 \\ 0 & e^{i\theta_2} & 0 \\ 0 & 0 & 1 \end{bmatrix} E^{(i)} \right|^2 = \left| T' \begin{bmatrix} e^{i\theta_1} \\ e^{i\theta_2} \\ 1 \end{bmatrix} \right|^2,$$

where

$$T' = T \begin{bmatrix} E_1^{(i)} & 0 & 0 \\ 0 & E_2^{(i)} & 0 \\ 0 & 0 & E_3^{(i)} \end{bmatrix}.$$

This brings us back to a classical optimization problem, but with a new matrix  $T'$ .

## II. OPTIMIZATION OF A TWO-PHOTON STATE

In this section, we investigate the space of solutions that maximize correlations in the case of a two-photon state propagating through a scattering medium.

### A. Reduction of the parameter space

Equation (1) in the manuscript corresponds to one row of the matrix equation describing the propagation of a two-photon state through a scattering medium:

$$\psi^{(o)} = T\psi^{(i)}T^t, \quad (\text{B9})$$

where  $T$  is the scattering matrix and

$$\psi^{(i)} = \begin{bmatrix} \psi_{11}^{(i)} e^{i\theta_{11}} & \dots & \dots \\ \dots & \psi_{kl}^{(i)} e^{i\theta_{kl}} & \dots \\ \dots & \dots & \psi_{NN}^{(i)} e^{i\theta_{NN}} \end{bmatrix},$$

where  $N$  is the total number of input modes,  $\theta_{kl}$  are phase terms and  $\psi_{kl}^{(i)}$  represents the two-photon state coefficients. As seen in Equation (1) of the manuscript, in an ideal case, all  $N^2$  phase terms  $\theta_{kl}$  could be adjusted independently to maximize the correlation value between any pair of output modes, and the optimization problem would then be equivalent to the classical case. However, when using a single SLM, only  $N$  phase terms  $\theta_k$  corresponding to the  $N$  input modes can be controlled, leading to  $\theta_{kl} = \theta_k + \theta_l$ . In this scenario, the effective accessible parameter space is reduced and of smaller dimension.

For example, Figure S2a illustrates a simple case with two input modes and two output modes. If all the phases (i.e.,  $\theta_{11}$ ,  $\theta_{12}$ , and  $\theta_{22}$ ) can be controlled, the parameter space is two-dimensional, and the correlation map in Figure S2b shows a unique global maximum with no local maxima, similar to the classical case. However, in practice, only  $\theta_1$  and  $\theta_2$  can be controlled, reducing the parameter space to one dimension. As shown in Figure S2c, the variation of output correlations is a curve that does not necessarily reach the global maximum of the full parameter space (Fig S2b). It can exhibit local maxima and potentially multiple solutions.

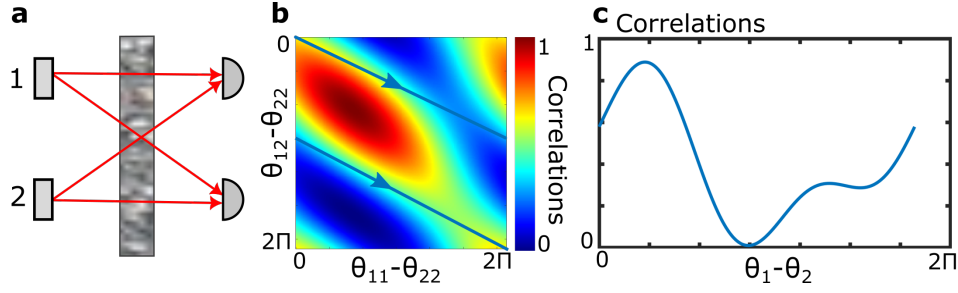


Figure S2. **Simulations of the parameter space for two-photon state propagation and shaping through a scattering medium.** **a**, A two-photon state propagates through a scattering medium. Two input spatial modes and two output spatial modes, between which the correlations are measured, are considered. The transmission matrix  $T$  is a  $2 \times 2$  matrix with random complex coefficients generated as  $T = \mathbf{rand}(2) \cdot \exp(i \cdot \mathbf{rand}(2) \cdot 2\pi)$ , where  $\mathbf{rand}$  is a MATLAB function. **b**, Correlation values  $\Gamma^{(o)}(\theta_{11}, \theta_{12})$  are calculated assuming full control over the phase terms  $\theta_{11}$ ,  $\theta_{12}$ , and  $\theta_{22}$  (with  $\theta_{11} + \theta_{12} + \theta_{22} = \text{constant}$ ). The blue line represents the reduced parameter space under the experimental constraint that only two phases,  $\theta_1$  and  $\theta_2$ , can be arbitrarily controlled (with  $\theta_1 + \theta_2 = \text{constant}$ ). The relationship between the phase terms is  $\theta_{11} = 2\theta_1$ ,  $\theta_{12} = \theta_1 + \theta_2$ , and  $\theta_{22} = 2\theta_2$ . **c**, Correlation values as a function of  $\theta_1 - \theta_2$  (i.e. corresponding to the blue line in **(b)**), revealing that local maxima can exist, and that the global maximum here does not necessarily reach the global maximum of the full parameter space.

### B. Influence of the input two-photon field

As we have seen in the previous section, the parameter space accessible in practice is reduced. In particular, the properties of this space depends on the form of the input state incident on the SLM. To illustrate this, Figure S3 presents simulations of a simple case with 3 input modes and 2 output modes. In these simulations, the same scattering matrix, composed of  $3 \times 2$  random complex coefficients, is generated. Parameter spaces are then calculated, and an iterative optimization is performed for three different forms of input states:

- Figure S3b shows the output correlation rates in function of  $\theta_1 - \theta_3$  and  $\theta_2 - \theta_3$  for an input state of the form  $|\Psi\rangle = 1/\sqrt{3}[a_1^{\dagger 2} + a_2^{\dagger 2} + a_3^{\dagger 2}]|0\rangle$ . In this case, we observe the presence of genuine multiple global maxima (i.e. identical values) of the output correlation, between which the optimization process can oscillate. This state is very similar to the one incident on the SLM when using the experimental configuration presented in Figure 2 of the manuscript.
- Figure S3c shows the output correlation rates in function of  $\theta_1 - \theta_3$  and  $\theta_2 - \theta_3$  for an input state of the form  $|\Psi\rangle = [0.577a_1^{\dagger 2} + 0.577a_2^{\dagger 2} + 0.577a_3^{\dagger 2} + 0.002a_1^{\dagger}a_2^{\dagger} + 0.002a_2^{\dagger}a_3^{\dagger}]|0\rangle$ . In this case, we observe the presence of global and local maxima with very similar correlation values. In practice, the presence of experimental noise makes them indistinguishable, and the optimization process can also oscillate between these different attractors.
- Figure S3d show the output correlation rates in function of  $\theta_1 - \theta_3$  and  $\theta_2 - \theta_3$  for an input state of the form  $|\Psi\rangle = [0.35a_1^{\dagger 2} + 0.35a_2^{\dagger 2} + 0.35a_3^{\dagger 2} + 0.16a_1^{\dagger}a_2^{\dagger} + 0.16a_2^{\dagger}a_3^{\dagger} + 0.002a_1^{\dagger}a_3^{\dagger}]|0\rangle$ . Here again, we observe the presence of local maxima with values approaching those of the global maxima.
- Figure S3e and f shows the output correlation rates in function of  $\theta_1 - \theta_3$  and  $\theta_2 - \theta_3$  for two different input state of the form  $|\Psi\rangle = \mathcal{N} \sum_{k=1}^3 \sum_{l=k}^3 \alpha_{kl} a_k^{\dagger} a_l^{\dagger} |0\rangle$ , where  $\alpha_{kl}$  are random complex coefficients and  $\mathcal{N}$  is a normalization factor. We clearly observe that the parameter space strongly depends on the form of the input state. In Figure S3e, it presents multiple maxima of similar values between which the optimization can oscillate. In Figure S3e, however, there is only one clear maximum to which the optimization always converges.

These simulations highlight the complexity of the reduced parameter space when using a single SLM to shape a two-photon state. In particular, they confirm that local maxima and multiple global maxima can exist, but their presence strongly depends on the form of the two-photon input state shaped by the SLM. In our experimental configuration, the crystal and the SLM are positioned so that the two-photon state incident on the SLM is not random but has a shape of the approximate form:  $|\Psi\rangle = \left[ J_0 \sum_{k=1}^N a_k^{\dagger 2} + J_1 \sum_{k=1}^{N-1} a_k^{\dagger} a_{k+1}^{\dagger} + J_2 \sum_{k=1}^{N-2} a_k^{\dagger} a_{k+2}^{\dagger} + \dots \right] |0\rangle$ , with  $J_n \gg J_{n+1}$ . we are therefore operating in a situation close to those simulated in Figures S3b-d, where multiple maxima of similar values seems to always exist.

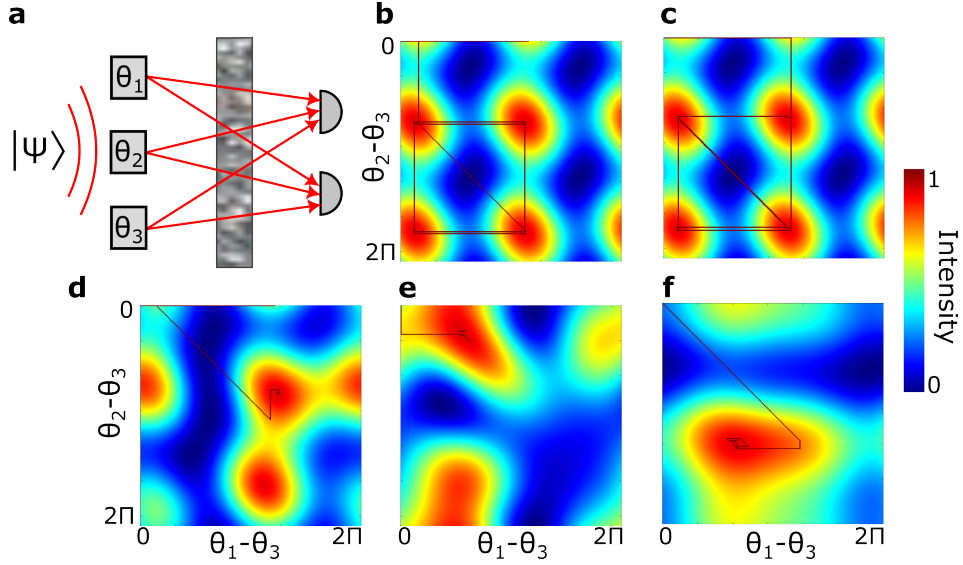


Figure S3. **Simulations of iterative optimizations for different input states propagating through the same scattering medium.** **a**, A two-photon state propagates through a scattering medium. Three input spatial modes and two output spatial modes, between which the correlations are measured, are considered. The transmission matrix  $T$  is a  $2 \times 3$  matrix with random complex coefficients, generated as  $T = \text{rand}(2, 3) \cdot \exp(i \cdot \text{rand}(2, 3) \cdot 2\pi)$ , where  $\text{rand}$  is a MATLAB function. Correlation values  $\Gamma^{(o)}(\theta_{11}, \theta_{12})$  are plotted as a function of  $\theta_1 - \theta_2$  and  $\theta_1 - \theta_3$  for different input states incident on the SLM: **(b)**  $|\Psi\rangle = \mathcal{N}[a_1^{\dagger 2} + a_2^{\dagger 2} + a_3^{\dagger 2}]|0\rangle$ , **(c)**  $|\Psi\rangle = [0.577a_1^{\dagger 2} + 0.577a_2^{\dagger 2} + 0.577a_3^{\dagger 2} + 0.002a_1^{\dagger}a_2^{\dagger} + 0.002a_2^{\dagger}a_3^{\dagger}]|0\rangle$ , **(d)**  $|\Psi\rangle = [0.35a_1^{\dagger 2} + 0.35a_2^{\dagger 2} + 0.35a_3^{\dagger 2} + 0.16a_1^{\dagger}a_2^{\dagger} + 0.16a_2^{\dagger}a_3^{\dagger} + 0.002a_1^{\dagger}a_3^{\dagger}]|0\rangle$ , and **(e-f)**  $|\Psi\rangle = \mathcal{N} \sum_{k=1}^3 \sum_{l=k}^3 \alpha_{kl} a_k^{\dagger} a_l^{\dagger} |0\rangle$  with two different sets of  $\alpha_{kl}$ , which are random complex coefficients.  $\mathcal{N}$  is a normalization factor for each state. The red line represents the iterative optimization path in parameter space using a partitioning algorithm. In each optimization simulation, white noise with a variance of approximately 1% of the mean correlation value was added to mimic experimental noise.

### C. Influence of the scattering matrix

Figure S4 shows the parameter space for different scattering matrices, in the simple case of 3 input modes and 2 output modes. Interestingly, as shown in Figures S4a and S4b, when the input state is close to a maximally entangled state, i.e.,  $|\Psi\rangle \approx \mathcal{N}[a_1^{\dagger 2} + a_2^{\dagger 2} + a_3^{\dagger 2}]|0\rangle$ , there always exist maxima with very close values. As explained at the end of the previous subsection, in our work the SLM and the crystal are positioned in a configuration that approximately satisfies this condition. When the input state is random, however, Figures S4c and S4d confirm that the parameter space can be very different. It may or may not have multiple maxima with similar values, and it can lead to very complex optimization paths.

## III. ADDITIONAL DETAILS ON FINDING THE OPTIMAL PHASE VALUE

In this section, we provide an analytical method to find the maximum of the function  $\Gamma(\theta) = A \cos(2\theta + \theta_A) + B \cos(\theta + \theta_B) + C$  described in Equation (2) of the manuscript, where  $\theta \in [0, 2\pi[$  is the variable and  $\theta_A \in [0, 2\pi[$ ,  $\theta_B \in [0, 2\pi[$ ,  $A \geq 0$  and  $B \geq 0$ , and  $\theta_B$  are known parameters. These parameters are determined from experimental measurements using Equations (6), (7), and (8) or directly by fitting the data with the model in Equation (2). To find the maximum of  $\Gamma(\theta)$ , denoted  $\theta_{max}$ , we first set its derivative to zero:

$$\frac{d\Gamma}{d\theta} = -2A \sin(2\theta + \theta_A) - B \sin(\theta + \theta_B) = 0. \quad (\text{B10})$$

Then, let's eliminate some trivial solutions. If  $A = 0$ , then it is clear that  $\theta_{max} = -\theta_B$ . If  $B = 0$ , then there are two solutions:  $\theta_{max} = \{-\theta_A/2, -\theta_A/2 + \pi\}$ . If  $\theta_A = 2\theta_B + \pi$ , then  $\theta_{max} = -\theta_B + \pi/2$ . If  $\theta_A = 2\theta_B$ , then  $\theta_{max} = -\theta_B$ . If  $A \neq 0$  and  $B \neq 0$ , we can rewrite equation (B10) as follows:

$$\frac{1}{2} \sin(2x) + D \sin(x + \phi) = 0, \quad (\text{B11})$$

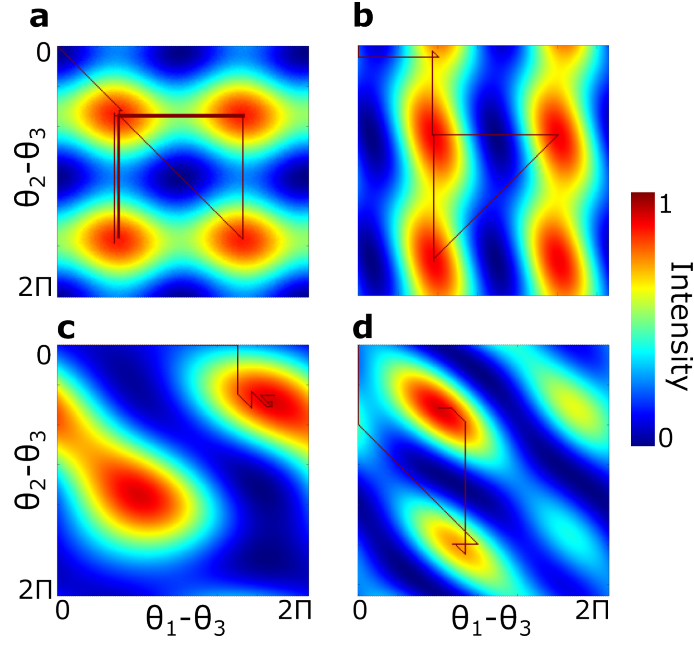


Figure S4. **Simulations of iterative optimizations with an input two-photon state for different scattering matrices.** In this simulation, we also consider the optical arrangement described as in Figure S3a. **a and b**, Correlation values  $\Gamma^{(o)}(\theta_{11}, \theta_{12})$  as a function of  $\theta_1 - \theta_2$  and  $\theta_1 - \theta_3$  for two different scattering matrices (generated as  $T = \text{rand}(2, 3) \cdot \exp(i \cdot \text{rand}(2, 3) \cdot 2\pi)$ ) and an input state incident on the SLM of the form  $|\Psi\rangle = \mathcal{N}[a_1^{\dagger 2} + a_2^{\dagger 2} + a_3^{\dagger 2}]|0\rangle$ . **c and d**, Correlation values for two different scattering matrices and an input state incident on the SLM of the form  $|\Psi\rangle = \sum_{k=1}^3 \sum_{l=k}^3 \alpha_{kl} a_k^{\dagger} a_l^{\dagger} |0\rangle$ , where  $\alpha_{kl}$  are random complex coefficients. The red line represents the iterative optimization path in parameter space using a partitioning algorithm. In each optimization simulation, white noise with a variance of approximately 1% of the mean correlation value was added to mimic experimental noise.

with the new variables  $x = (2\theta + \theta_A)/2$ ,  $D = B/(4A)$  and  $\phi = \theta_B - \theta_A/2$ . Equation (B11) then expands as

$$\begin{aligned} \frac{1}{2} \sin(2x) + D \sin(s + \phi) &= \cos(x) \sin(x) + D \sin(x) \cos(x) + D \cos(\phi) \sin(x) \\ &= XY + eX + fY = 0, \end{aligned} \quad (\text{B12})$$

with the new variables  $X = \cos(x)$ ,  $Y = \sin(x)$ ,  $e = D \sin(\phi)$  and  $f = D \cos(\phi)$ . The problem can thus be written in the form of a system of two equations:

$$\begin{cases} XY + eX + fY = 0 \\ X^2 + Y^2 = 1. \end{cases}$$

Then, we can write:

$$\begin{aligned} X(Y + e) + fY = 0 &\implies X = \frac{-fY}{Y + e} \\ &\implies \frac{f^2 Y^2}{(Y + e)^2} + Y^2 = 1 \\ &\implies Y^4 + 2eY^3 + [f^2 - 1 + e^2]Y^2 - 2eY - e^2 = 0, \end{aligned} \quad (\text{B13})$$

where the pathological case  $Y = -e$  corresponds to the trivial solutions  $\theta_A = 2\theta_B$  and  $\theta_A = 2\theta_B + \pi$ , which were already found previously. Finally, Equation (B13) is a degree-4 equation, which can be solved analytically. Once the different solutions are obtained (up to 4), they must be substituted into Equation (B10), and the one yielding the highest value is the (global) maximum. Note that it is also possible to find  $\theta_{max}$  using a numerical method.

#### IV. ADDITIONAL DETAILS ON THE EXPERIMENTAL SETUP

The pump is a collimated continuous-wave laser at 405 nm (Coherent OBIS-LX) with an output power of 100 mW and a beam diameter of  $0.8 \pm 0.1$  mm. The classical source is a superluminescent diode (SLED) centered at 810nm and has a total bandwidth of approximately 20nm (Superlum). BBO crystal has dimensions  $0.5 \times 5 \times 5$  mm and is cut for type I SPDC at 405 nm with a half opening angle of 3 degrees (Newlight Photonics). The crystal is slightly rotated around horizontal axis to ensure near-collinear phase matching of photons at the output (i.e. ring collapsed into a disk). A 650 nm-cut-off long-pass filter is used to block pump photons after the crystals, together with a band-pass filter centered at  $810 \pm 5$  nm. The SLM has  $1080 \times 1920$  pixels with a pitch of  $8\mu\text{m}$  and uses a liquid crystal on silicon technology (Holoeye model Pluto-NIR-II). The SLM is tilted and a phase ramp is continuously displayed on it to work with the first order of diffraction. The SPAD camera is the model SPC3 from Micron Photon Device. It has  $32 \times 64$  pixel, a pixel pitch of  $45\mu\text{m}$  and is operated in the snap-running mode with an exposure time of  $1\mu\text{s}$ . On the same plane as the SPAD, a CCD camera (uEye) with 1024 by 1280 pixel to perform measurement when the classical source is used. The  $4f$  imaging system  $f_1 - f_2$  in Figure 3.a is represented by two lenses for clarity, but is in reality composed of a series of 4 lenses with focal lengths 50 mm - 150 mm - 100 mm - 200 mm. The first and the last lens are positioned at focal distances from the crystal and the SLM, respectively, and the distance between two lenses in a row equals the sum of their focal lengths. The SPDC beam occupies an area of 300 by 300 pixels on the SLM plane. Similarly, the second  $4f$  imaging system  $f_3 - f_4$  in Figure 3.a is composed of a series of 4 consecutive lenses with focal lengths 200mm - 100 mm - 75 mm - 50 mm arranged as in the previous case. The other lenses have the following focal lengths:  $f_5 = 150\text{mm}$ .

#### V. DEMONSTRATION OF EQUATION (23) OF THE MANUSCRIPT

This section demonstrate Equation (23) of the manuscript. In our experimental configuration, the scattering medium is a thin layer of parafilm. It can thus be modelled by a complex function  $t(\mathbf{r})$ , where  $\mathbf{r}$  is the transverse position in the optical plane where the medium is placed. In this case, the output two-photon field  $\psi^{(o)}$  can be written as

$$\psi^{(o)}(\mathbf{r}'_1, \mathbf{r}'_2) = \int \psi^{(i)}(\mathbf{r}_1, \mathbf{r}_2) t(\mathbf{r}_1) t(\mathbf{r}_2) e^{-\frac{\mathbf{r}'_1 \cdot \mathbf{r}_1}{\lambda f}} e^{-\frac{\mathbf{r}'_2 \cdot \mathbf{r}_2}{\lambda f}} d\mathbf{r}_1 d\mathbf{r}_2, \quad (\text{B14})$$

where  $\psi^{(i)}$  is the input two-photon field in the medium plane,  $\lambda$  nm is the photons wavelength,  $f = f_5 f_3 / f_4$ , and  $\mathbf{r}'_1$ ,  $\mathbf{r}'_2$  and  $\mathbf{r}_1$ ,  $\mathbf{r}_2$  are the transverse positions in the camera and medium planes, respectively.  $\psi^{(i)}$  can be approximated by a Double-Gaussian [41],  $\psi^{(i)}(\mathbf{r}_1, \mathbf{r}_2) \propto \exp\left(\frac{-|\mathbf{r}_1 - \mathbf{r}_2|^2}{4\sigma_r^2}\right) \exp\left(\frac{-|\mathbf{r}_1 + \mathbf{r}_2|^2 \sigma_k^2}{4}\right)$ , where  $\sigma_r$  and  $\sigma_k$  are the position and momentum correlation widths, respectively. If  $\sigma_r$  is smaller than the typical transverse spatial correlation length of the medium (i.e. its roughness), Equation B14 simplifies to

$$\psi^{(o)}(\mathbf{r}'_1, \mathbf{r}'_2) \approx g * \mathcal{F}[t^2](\mathbf{r}'_1 + \mathbf{r}'_2), \quad (\text{B15})$$

where  $\mathcal{F}$  denotes a Fourier transform and  $g(\mathbf{r}) = \exp(-|\mathbf{r}|^2/4\Sigma)$ , with  $\Sigma$  being the width of the beam in the medium plane. As a result,  $\psi^{(o)}$  and, thus,  $\Gamma$ , are functions of a single variable  $\mathbf{r}_1 + \mathbf{r}_2$ . After discretization, one can conclude that all the values  $\Gamma_{c-k, c+k}$ , i.e. the correlation values between the pixel pairs  $c - k$  and  $c + k$  (which are symmetric with respect to an arbitrarily chosen pixel  $c$ ), are all the same.

#### VI. NON-CLASSICAL OPTIMIZATION THROUGH THICKER SCATTERING MEDIA AND CHOICE OF THE OPTIMIZATION TARGET ( $\Gamma_{kl}$ OR $\Gamma_T^+$ ).

To maintain a sufficient signal-to-noise ratio (SNR) during our measurements, the experiments shown in Figures 1, 2, 3a-f, and 5 of the manuscript were conducted using thin scattering media. Indeed, the use of thin media not only (i) allows for a sufficiently high photon pair flux collected in transmission, but also (ii) enables measuring the sum-coordinate projection  $\Gamma^+$  instead of directly measuring the coincidence rate  $\Gamma_{kl}$  between two camera pixels  $k$  and  $l$ , resulting in an increased SNR by a factor of  $M \sim 1000$ . However, using a thin medium is not a prerequisite for implementing non-classical optimization. Directly optimizing  $\Gamma_{kl}$  also works, provided the experimental SNR is sufficient. In this section, we present both simulation and experimental results using  $\Gamma_{kl}$  as an optimization target for both thin and thick scattering media, confirming that our conclusions hold regardless of the type of scattering medium. In particular, we demonstrate that the optimization also converges to phase masks that do not focus classical coherent light.

- Figure S5.a-d show simulation results for optimizing the coincidence rate between two arbitrarily selected output modes of a thin scattering medium. The input state incident on the SLM is simulated using a Double-Gaussian model [41], with parameters experimentally determined in Section VII. The transmission matrix used in the simulations was experimentally measured using classical coherent light and a thin scattering medium (one parafilm layer), using the method described in Ref. [26]. Figure S5.a shows the enhancement of the coincidence rate between two output pixels,  $k$  and  $l$ , with respective positions  $(x_k, y_k) = (10, 15)$  and  $(x_l, y_l) = (17, 42)$ , as a function of the number of steps in the iterative algorithms. After optimization,  $\Gamma_{kl}$  reveals an enhancement of the coincidence rate around specific positions (Figure S5.c), confirming the success of the optimization.
- Figures S5e-h and S5i-l show similar simulation results for a thicker scattering medium and a 'perfectly random' scattering medium, respectively. To simulate the thicker medium, we used an experimentally measured transmission matrix of a six-layer parafilm stack. For the 'perfectly random' scattering medium, the scattering matrix was generated using MATLAB's `rand` function. In both cases, the iterative optimization successfully enhanced the coincidence rate between the selected output pair of pixels (Figs. S5g and k). The intensity images obtained after optimization, when the photon pair source was replaced by classical coherent light, do not show any focusing points for either situation (Figs. S5h and j).
- Figures S6a-c show hybrid experiment-simulation results for a thicker scattering medium. In this case, a transmission matrix of a six-layer parafilm stack was first measured using classical coherent light. Then, the optimization of  $\Gamma_{kl}$  was simulated on the computer using a two-photon state at the input, resulting in a phase mask shown in Figure S6a and the correlation image in Figure S6b. It confirms the success of the maximization of the coincidence rate between modes  $k$  and  $l$ . This phase mask was then programmed on the SLM of the experiment operated with classical coherent light. This leads to a speckle pattern at the output, confirming again experimentally that this phase mask does not refocus the classical light.
- Figures S6d-f show results similar to those obtained in Figures 3g-i of the manuscript, but with optimization on  $\Gamma_{kl}$  instead of the sum-coordinate projection. This experiment reproduces the correlations that would be obtained with a non-entangled state using classical coherent light, by multiplying the intensity values at the output i.e.  $\Gamma_{kl} = |E_k^{(o)}|^2 |E_l^{(o)}|^2$ . In this case, there is sufficient SNR to conduct the experiment without relying on simulations. Figure S6d shows the optimal phase mask obtained. Figure S6e shows the correlation image  $\Gamma_{kl}$ , revealing the focii at the modes  $k$  and  $l$ . Finally, Figure S6f shows the intensity image where two focii also appear at modes  $k$  and  $l$ , further confirming that the optimization performed on the correlations of a non-entangled state inevitably leads to focusing of classical light on the output modes in intensity.

These results confirm that, even though for practical reasons we used our algorithm to optimize the correlations at an arbitrary position of the sum-coordinate projection of  $\Gamma$ , our approach also works if we optimize the coincidences rate between a single pair of pixels, regardless of the complexity of the scattering media.

## VII. CHARACTERIZATION OF THE TWO-PHOTON STATE IN THE SLM PLANE

### A. Experimental characterization

The two photon state  $\psi(\mathbf{r}_1, \mathbf{r}_2)$  produced by a Type-I thin non linear crystal can be expressed analytically using the double Gaussian model [42]:

$$\psi(\mathbf{r}_1, \mathbf{r}_2) = A \exp\left\{\left(\frac{-|\mathbf{r}_1 - \mathbf{r}_2|^2}{4\sigma_{\mathbf{r}}^2}\right)\right\} \exp\left\{\left(\frac{-|\mathbf{r}_1 + \mathbf{r}_2|^2 \sigma_{\mathbf{k}}^2}{4}\right)\right\}, \quad (\text{B16})$$

where  $\sigma_{\mathbf{r}}$  and  $\sigma_{\mathbf{k}}$  are the position and momentum correlation widths, respectively. To determine their values in our experimental setup, we used an EMCCD camera and the method detailed in Refs. [43, 44].

For  $\sigma_{\mathbf{r}}$ , we added a lens with  $f_6 = 30$  mm between the last lenses  $f_4$  and  $f_5$ , setting all lens pairs in a  $4f$  configuration, in order to image the surface of the crystal onto the camera (Figure 3a of the manuscript). Figures S7a and b show the intensity image and the minus-coordinate projection of the second-order correlation function, respectively. The width of the peak in Figure S7b corresponds to the position correlation width  $\sigma_{\mathbf{r}}$ . It is estimated to be 3 pixels using a Gaussian fit, as shown in Figure S7c. Taking into account that the magnification between the SLM and the camera is  $5/3$  and that the camera pixel size is 16 micrometers, we find that the position correlation width in the SLM plane is  $\sigma_{\mathbf{r}} \approx 2.9 \cdot 10^{-5}$  m.

$\sigma_{\mathbf{k}}$  is estimated directly from the width  $\Sigma$  of the intensity image shown in Figure S7a, again using a Gaussian fit. Indeed, this width is directly related to  $\sigma_{\mathbf{k}}$  by the formula  $\sigma_{\mathbf{k}} = 1/\sqrt{\Sigma^2 - \sigma_{\mathbf{r}}^2}$  [42]. Taking into account the

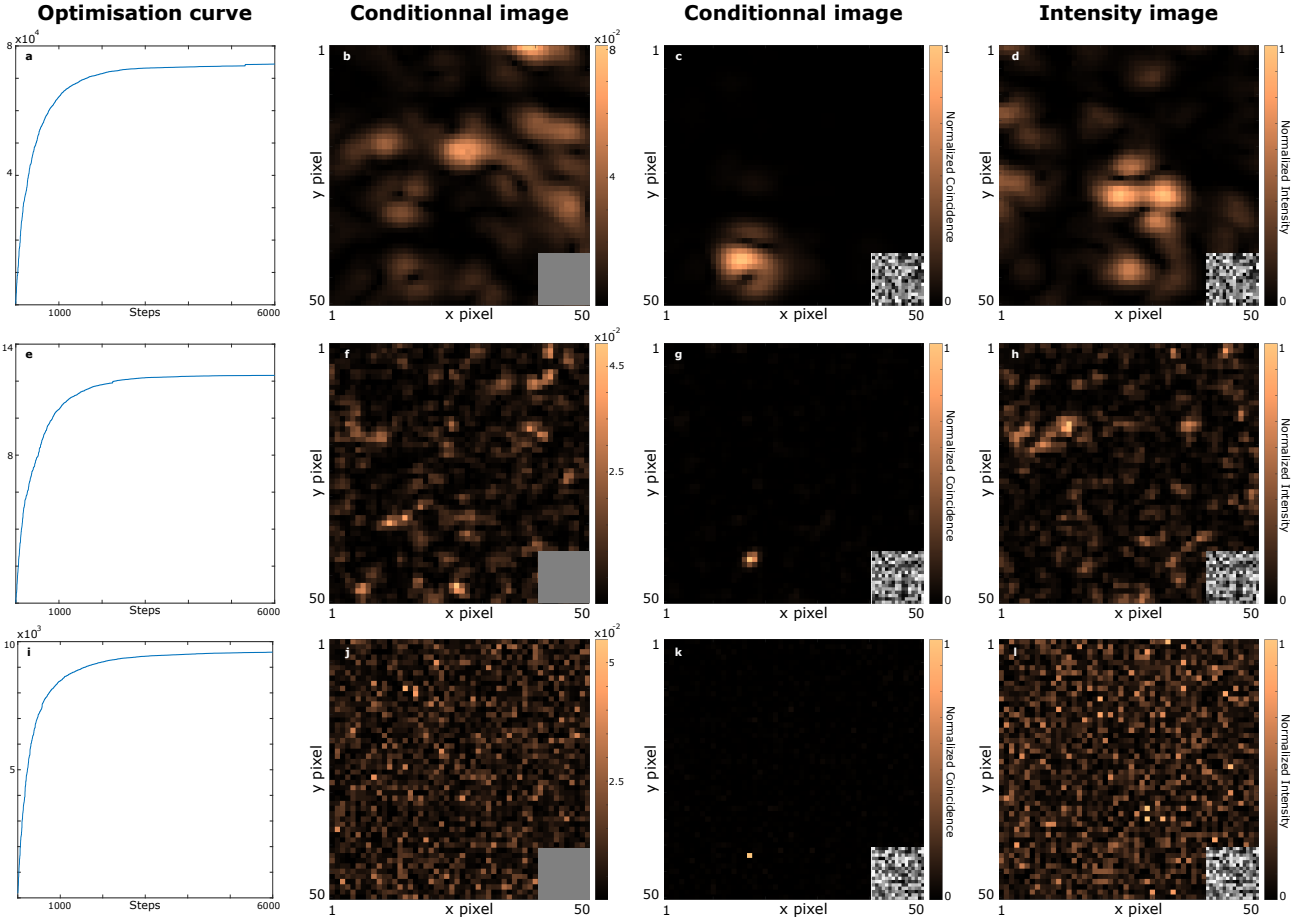


Figure S5. **Simulation of focusing entangled photons into two arbitrary spatial modes for thin and thick scattering media.** **a-d**, The simulation is performed using an experimentally measured scattering matrix of a thin scattering medium (one layer of parafilm) and an input state with the same properties as the one used in our experiment. **a**, Optimization curve using  $\Gamma_{kl}$  as a target, with respective positions  $(x_k, y_k) = (10, 15)$  and  $(x_l, y_l) = (17, 42)$ . **b**, Conditional image  $\Gamma_{x,y|l}$  with a flat phase mask on the SLM. **c**, Conditional image  $\Gamma_{x,y|l}$  at the end of the optimization (optimal phase mask in inset). **d**, Output intensity observed after replacing photon pairs with classical coherent light, showing no focus. **e-h**, The simulation is performed using an experimentally measured scattering matrix of a thick scattering medium (six layers of parafilm) and an input state with the same properties as the one used in our experiment. **e**, Optimization curve using  $\Gamma_{kl}$  as a target, with respective positions  $(x_k, y_k) = (10, 15)$  and  $(x_l, y_l) = (17, 42)$ . **f**, Conditional image  $\Gamma_{x,y|l}$  with a flat phase mask on the SLM. **g**, Conditional image  $\Gamma_{x,y|l}$  at the end of the optimization (optimal phase mask in inset). **h**, Output intensity observed after replacing photon pairs with classical coherent light, showing no focus. **i-l**, The simulation is performed using a scattering matrix generated using MATLAB's `rand` function, modeling a perfectly random scattering medium, and an input state with the same properties as the one used in our experiment. **i**, Optimization curve using  $\Gamma_{kl}$  as a target, with respective positions  $(x_k, y_k) = (10, 15)$  and  $(x_l, y_l) = (17, 42)$ . **j**, Conditional image  $\Gamma_{x,y|l}$  with a flat phase mask on the SLM. **k**, Conditional image  $\Gamma_{x,y|l}$  at the end of the optimization (optimal phase mask in inset). **l**, Output intensity observed after replacing photon pairs with classical coherent light, showing no focus. All the transmission matrices used in these simulations connect  $16 \times 16$  input modes (SLM macropixels) to  $100 \times 100$  output modes (CCD camera pixels). To reduce computational memory requirements, we focus exclusively on the central  $50 \times 50$  pixels region at the output.

magnification and the pixel size, we find  $\sigma_{\mathbf{k}} \approx 8.0 \cdot 10^2 \text{ m}^{-1}$ . Note that it is also possible to measure  $\sigma_{\mathbf{k}}$  directly by Fourier-imaging the crystal onto the EMCCD camera, as shown in Figures S7d-f.

## B. Discretization of $\psi$ on the SLM macropixels

In our experiments, each input spatial mode corresponds to an SLM macropixel composed of  $37 \times 37$  pixels, which corresponds to a square of approximately  $300 \cdot 10^{-5} \text{ m}$  width. However, as mentioned above, the position correlation width in the SLM plane is  $\sigma_{\mathbf{r}} \approx 2.9 \cdot 10^{-5} \text{ m}$ . Since the position correlation width is much smaller than the SLM

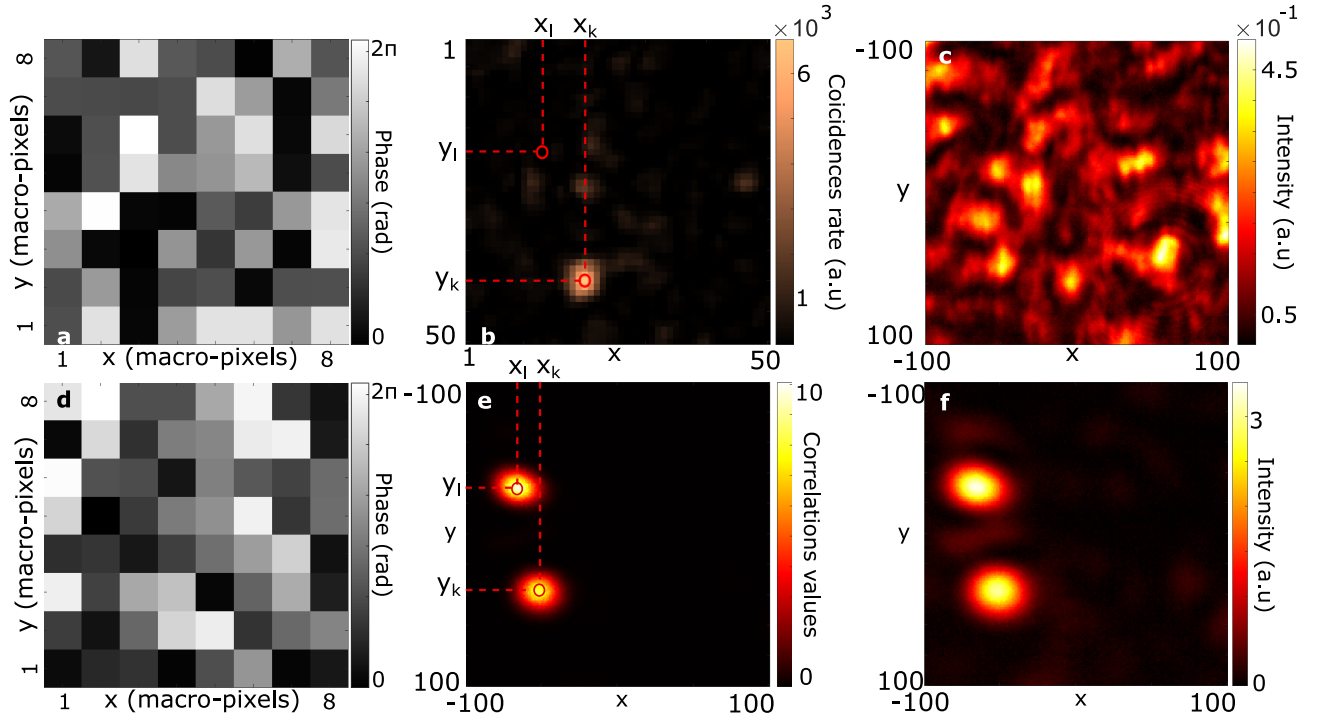


Figure S6. **Simulation and experiment of focusing entangled and non-entangled photons into two arbitrary spatial modes for a thick scattering medium.** **a-c** The simulation is performed using an experimentally measured scattering matrix of a thick scattering medium (six-layer parafilm stack) and an input state with the same properties as the one used in our experiment.  $\Gamma_{kl}$  is used as a target, with respective positions  $(x_k, y_k) = (10, 15)$  and  $(x_l, y_l) = (17, 42)$ . **a**, Optimal phase mask obtained after optimization. **b**, Conditional image  $\Gamma_{x,y|l}$  (simulation). **c**, Output intensity observed after programming the phase mask of the SLM and performing the experiment with classical coherent light, showing no focus. **d-f** To reproduce the result that would be obtained using a non-entangled state, an experiment is performed using classical coherent light propagating through the scattering medium. The optimization is performed using the product of the intensities at positions  $(x_k, y_k) = (10, 15)$  and  $(x_l, y_l) = (17, 42)$  as the target. The experimental conditions are the same as those used to obtain the results shown in Figures 3g-i of the manuscript. **d**, Optimal phase mask obtained after optimization. **e**, Conditional image  $\Gamma_{x,y|l}$  (experiment). **f**, Output intensity, showing two foci (experiment).

macropixel width, we can approximate that the discretized two-photon wave function  $\psi_{nm}^{(i)}$  in the macropixel basis mainly contains nonzero coefficients along its diagonal,  $\psi_{nn}^{(i)} \neq 0$ , and along the off-diagonals associated with coupling between directly neighboring pixels,  $\psi_{nm+1}^{(i)} \neq 0$ , while other terms are negligible. The intensity of the off-diagonal coefficients relative to the diagonal ones is estimated by the ratio of the position correlation width to the SLM macropixel size,  $29/300 \approx 0.1$ . We can thus simplify the discretized two-photon function (not normalized) as follows:

$$\psi_{nm}^{(i)} \approx \delta_{n-m} + \alpha \delta_{n-m+1}, \quad (\text{B17})$$

where  $n$  and  $m+1$  denote directly neighboring macropixels on the SLM.

Note that Equation (B17) has a very simplified form, as it corresponds to an SLM that would be one-dimensional. To account for the two-dimensional nature, i.e. the fact that each macropixel is actually coupled to 8 neighbors, additional terms must be included:

$$\begin{aligned} \psi_{nm}^{(i)} \approx & \delta_{n-m} + \alpha(\delta_{n-(m+1)} + \delta_{n-(m-1)} + \delta_{n-(m+\sqrt{N})} + \delta_{n-(m-\sqrt{N})}) \\ & + \alpha'(\delta_{n-(m+\sqrt{N}-1)} + \delta_{n-(m+\sqrt{N}+1)} + \delta_{n-(m-\sqrt{N}-1)} + \delta_{n-(m-\sqrt{N}+1)}), \end{aligned} \quad (\text{B18})$$

where  $\alpha'$  is another coupling coefficient between diagonally neighboring pixels, and  $N$  is the number of SLM macropixels considered, forming a square of  $\sqrt{N} \times \sqrt{N}$ .

However, in the context of our work, there is no particular interest in using such a complex expression. To demonstrate Equation (4) (see also Supplementary Section X), we therefore simply consider Equation (B17).

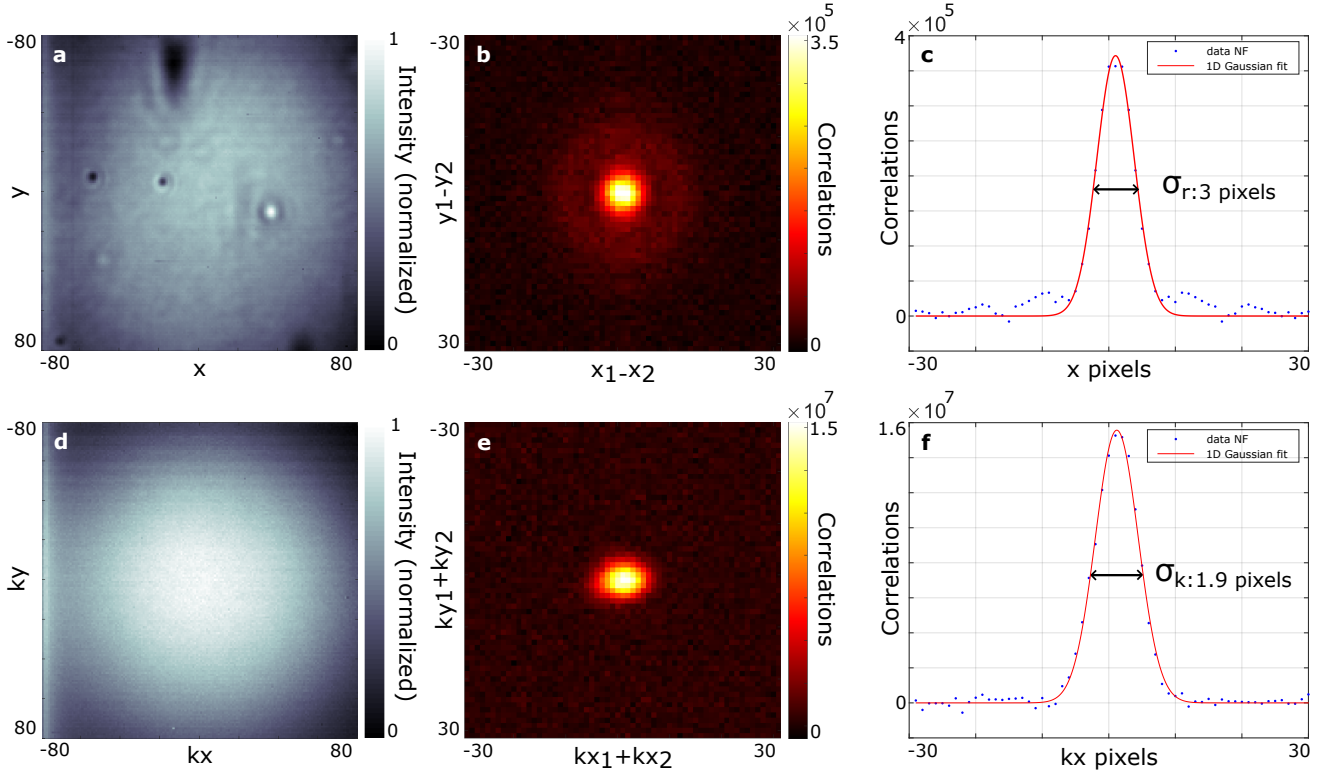


Figure S7. **Experimental measurements of position and momentum correlation widths.** **a** and **b**, Intensity image and minus-coordinate projection of the second-order correlation function when imaging the surface of the crystal on an EMCCD camera. **c**, Fitting the peak in the minus-coordinate projection with a Gaussian returns a position correlation width of 3 pixels. The corresponding value in the SLM plane is calculated by considering the magnification between the SLM and camera planes and the camera pixel size, resulting in  $\sigma_r \approx 2.9 \cdot 10^{-5}$  m. Using a Gaussian fit on the intensity image, the total width  $\Sigma \approx 130$  pixels is found, allowing us to determine  $\sigma_k \approx 8.0 \cdot 10^2$  m $^{-1}$ . **d-f**,  $\sigma_k$  can also be estimated directly by Fourier-imaging the crystal on the EMCCD camera, replacing the SPAD camera in the configuration shown in Figure 3a of the manuscript. In this configuration, we measure the intensity image (**d**) and the sum-coordinate projection of the second-order correlation function (**e**). The width of the peak in the latter allows us to determine a width of approximately 1.9 pixels using a Gaussian fit (**f**). When converted to the SLM plane, the value is consistent with the one directly measured from the intensity image.

### VIII. CONSISTENCE OF THE OBSERVATION

To verify that the main conclusion of our study — non-classical optimization leads to a phase mask that does not refocus classical light — is not an isolated result, we have of course (1) reproduced the optimization experiment with several scattering media (including some shown in Figure S9 in the next section), but also (2) conducted numerous simulations, as the latter are much faster to perform than the experiments.

For example, we performed a batch of 10 additional simulations. In each simulation, the target was set to the central pixel of the sum-coordinate projection, and the input state matched the one used in the experiment. The scattering matrix used for these simulations corresponds to two layers of parafilm separated by 2cm. Figures S8a-c show the intensity images obtained at the end of the optimization for three of these simulations, each showing a distinct speckle pattern. Figures S8d-f show the respective sum-coordinate projections, all of which exhibit a strong peak at the central pixel, confirming the success of the optimization.

We observe, as expected, that when the non-classical optimization is repeated multiple times for a given medium and input state, a non-classical solution is always obtained. However, it is interesting to note that these solutions are always different from one another. To quantitatively assess these differences, we calculate the similarity between all possible pairs of intensity and sum-coordinate images obtained using MATLAB's `Corr2` function. The average similarity value between each sum-coordinate projection obtained at the end of the optimization is  $C_q = 0.971 \pm 0.007$ , confirming a high degree of consistency among the images (i.e. all the sum-coordinate projection at the end of the optimization look the same). In contrast, for the classical intensity images, the average similarity is  $C_c = 0.150 \pm 0.032$ , confirming significant differences between the non-classical solution obtained (i.e. all the classical intensity images

obtained at the end of the optimization are different). The different optimization simulations used to compute the correlation value are illustrated in Fig. S9. The convergence of the target pixel value from different initial conditions toward a common asymptotic limit suggests the presence of multiple local minima with close energy.

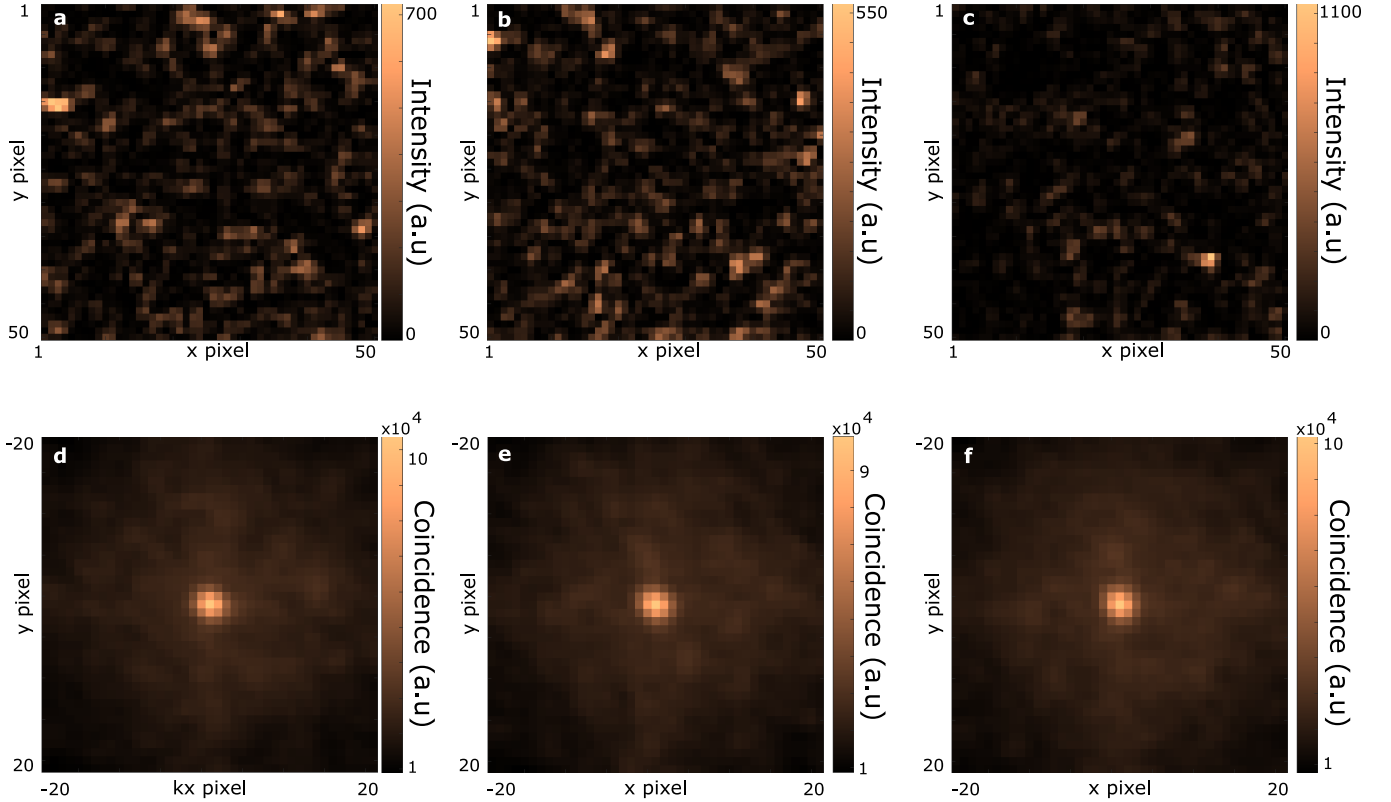


Figure S8. **Simulations to assess the consistency of the experiment.** (a-c) Intensity images and (d-f) obtained at the end of the optimization process for three simulations performed using the same scattering matrix and input state.

## IX. INFLUENCE OF THE NUMBER OF CONTROLLED INPUT MODES ON THE OPTIMIZATION PROCESS

When focusing through a scattering medium, a key parameter for evaluating the efficiency of the method is the enhancement factor at the end of the process i.e. once a plateau is reached. For classical optimization, this enhancement factor scales linearly with the number of modes controlled by the SLM, as detailed in Ref. [1]. A similar scaling is expected to be observed in the non-classical optimization case, as suggested in Ref. [19]. To confirm this, we perform the non-classical optimization for different numbers of input modes i.e. SLM macropixels. The results for three configurations are shown in Figure S10.a: the blue curve corresponds to an active area of  $4 \times 4$  macropixels, the red curve (as presented in the main text) corresponds to  $8 \times 8$ , and the violet curve corresponds to  $16 \times 16$ .

In the  $4 \times 4$  case, the algorithm reaches a plateau quickly, within just 40 steps ( $\sim 1$  day of acquisition). The enhancement factor for this configuration is computed to be  $\eta \approx 3$ . For the  $8 \times 8$  case, the plateau was achieved after 200 steps with an enhancement factor computed to be  $\eta \approx 5$  ( $\sim 5$  days of acquisition). For the  $16 \times 16$  case, even after 400 steps (more than 10 days!), the plateau had not been reached. At this point, we decided to halt the experiment. Based on the shape of the optimization curve in this final scenario, we are confident that the plateau, when reached, will be higher than that observed for the  $8 \times 8$  case.

While we do not have enough data to determine the precise scaling between the enhancement factor and the number of input modes, these experiments still confirmed that the larger the number of controlled input modes, the higher the enhancement factor. From a practical standpoint, these experiments primarily allowed us to favor the  $8 \times 8$  configuration in all our experiments, as it provides the optimal trade-off between acquisition time and enhancement factor.

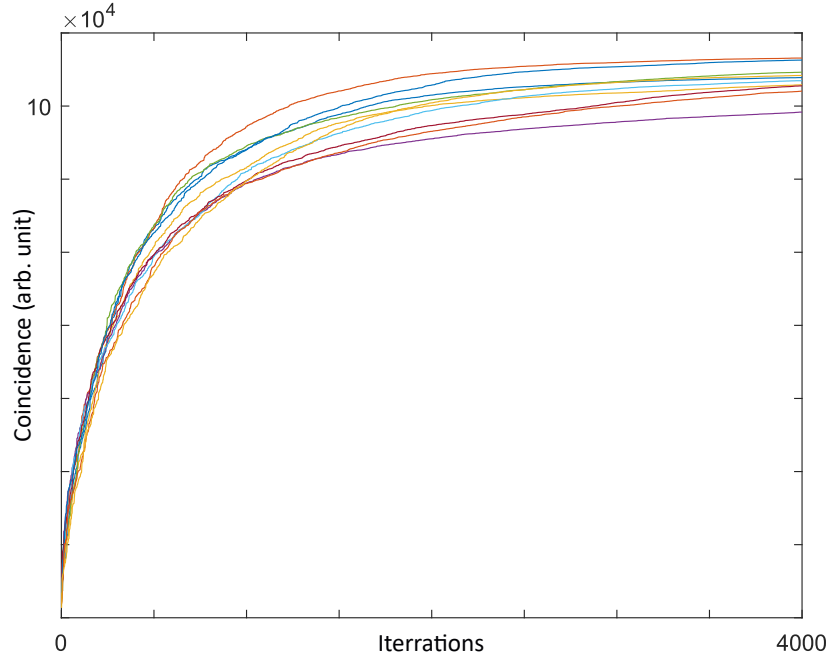


Figure S9. **Optimization curves for various initial phase masks.** Each curve represents an optimization process using the same quantum state properties and transmission matrix, but with different initial configurations of the SLM mask.

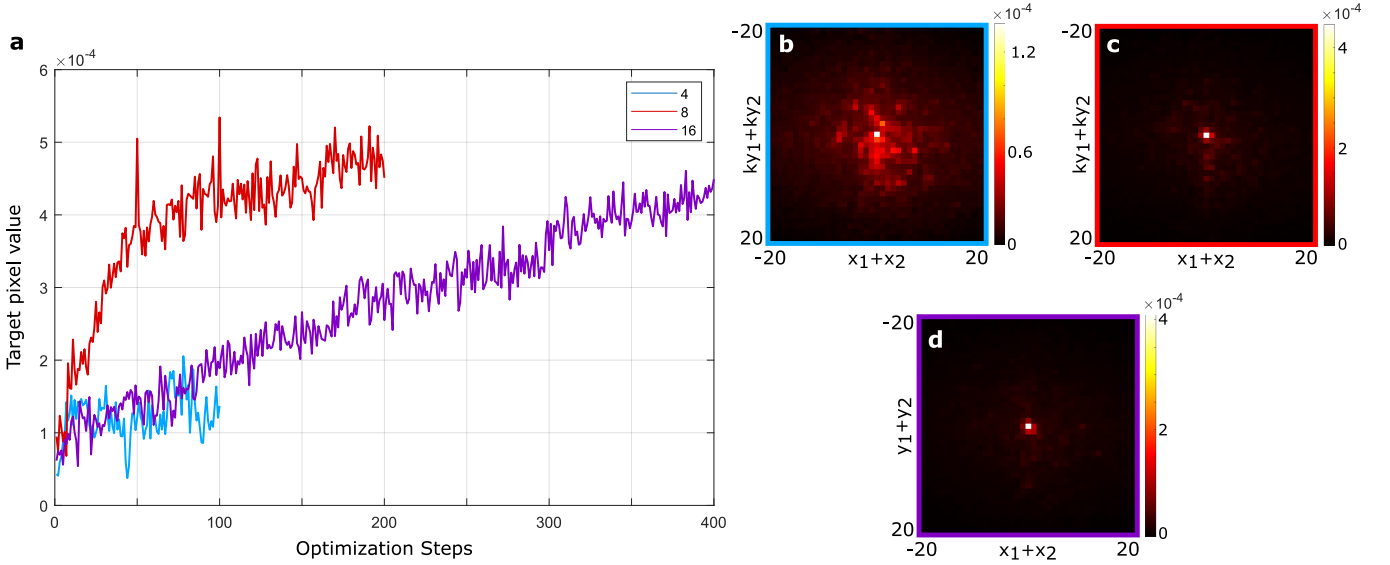


Figure S10. **Non-classical optimizations for various number of controlled input modes.** **a**, Experimentally measured optimization curves for  $4 \times 4$  SLM macropixels (blue curve),  $8 \times 8$  macropixels (red curve) and  $16 \times 16$  macropixels (violet curve). **b-d**, Sum coordinate projections obtained at the end of the optimization process in each case.

## X. DEMONSTRATION OF EQUATION (4) OF THE MANUSCRIPT - SPIN-GLASS MODEL WITH MULTI-SPIN INTERACTION

To demonstrate Equation (4) in the manuscript, we start from Equation (1) and proceed step by step: In our experimental configuration, we use a single SLM to shape the input two-photon field. As a result, the term  $e^{i\theta_{nm}}$  in Equation (1) of the manuscript is replaced by the product  $e^{i\theta_n} e^{i\theta_m}$ , where  $\theta_n$  is the phase value set at the input spatial mode  $n$  (i.e. the  $n^{\text{th}}$  SLM macropixel). Then, considering a phase encoding in 0 and  $\pi/2$ , Equation (1) simplifies as

follows:

$$\Gamma_{kl} = \left| \sum_{m,n} t_{km} t_{ln} \psi_{mn}^{(i)} \epsilon_m \epsilon_n \right|^2, \quad (\text{B19})$$

where  $\epsilon_n \in \{1, i\}$ .

Using the approximation  $\psi_{mn}^{(i)} \approx \delta_{m-n} + \alpha \delta_{m-n+1}$ , where  $\alpha \approx 0.1$  (see Supplementary Section VII A), Equation (B19) simplifies as follows:

$$\Gamma_{kl} = \left| \sum_n t_{kn} t_{ln} \epsilon_n^2 + \alpha \sum_n t_{kn} t_{l,n+1} \epsilon_n \epsilon_{n+1} \right|^2. \quad (\text{B20})$$

Using the relation  $\epsilon_n^2 = \sigma_n$ , it simplifies in,

$$\Gamma_{kl} = \left| \sum_n t_{kn} t_{ln} \sigma_n + \alpha \sum_n t_{kn} t_{l,n+1} \epsilon_n \epsilon_{n+1} \right|^2. \quad (\text{B21})$$

We then expand the absolute value of the sum of these terms into,

$$\begin{aligned} \Gamma_{kl} &= \sum_{nm} t_{kn} t_{ln} t_{km}^* t_{lm}^* \sigma_n \sigma_m \\ &\quad + \alpha \operatorname{Re} \left( \sum_{nm} t_{kn} t_{ln} t_{km}^* t_{lm+1}^* \sigma_n \epsilon_m^* \epsilon_{m+1}^* \right) \\ &\quad + \alpha^2 \sum_{nm} t_{kn} t_{ln+1} t_{km}^* t_{lm+1}^* \epsilon_n \epsilon_{n+1} \epsilon_m^* \epsilon_{m+1}^*. \end{aligned} \quad (\text{B22})$$

Expressing the  $\epsilon$ 's into spins, we obtain the relation,

$$\epsilon_n \epsilon_m = \frac{1}{2} (\sigma_n + \sigma_m) + \frac{i}{2} (1 - \sigma_n \sigma_m). \quad (\text{B23})$$

Inserting this into the second term of Equation B22, we obtain,

$$\operatorname{Re} \left( \sum_{nm} t_{kn} t_{ln} t_{km}^* t_{lm+1}^* \sigma_n \epsilon_m^* \epsilon_{m+1}^* \right) = \operatorname{Re} \left( \sum_{nm} t_{kn} t_{ln} t_{km}^* t_{lm+1}^* ((\sigma_n \sigma_m + \sigma_n \sigma_{m+1} - i (\sigma_n - \sigma_n \sigma_m \sigma_{m+1})) \right). \quad (\text{B24})$$

Let  $c_{nm}^{kl} = \operatorname{Re} (t_{kn} t_{ln} t_{km}^* t_{lm+1}^*)$  and  $d_{nm}^{kl} = \operatorname{Im} (t_{kn} t_{ln} t_{km}^* t_{lm+1}^*)$ , we can rewrite the second term as,

$$\operatorname{Re} \left( \sum_{nm} t_{kn} t_{ln} t_{km}^* t_{lm+1}^* \sigma_n \epsilon_m^* \epsilon_{m+1}^* \right) = \sum_{nm} c_{nm}^{kl} (\sigma_n \sigma_m + \sigma_n \sigma_{m+1}) + d_{nm}^{kl} (\sigma_n - \sigma_n \sigma_m \sigma_{m+1}). \quad (\text{B25})$$

Rewriting the third term of Equation B22 in terms of spins, we obtain,

$$\sum_{nm} t_{kn} t_{ln+1} t_{km}^* t_{lm+1}^* \epsilon_n \epsilon_{n+1} \epsilon_m^* \epsilon_{m+1}^* = \sum_{nm} a_{nm}^{kl} \operatorname{Re} (\epsilon_n \epsilon_{n+1} \epsilon_m^* \epsilon_{m+1}^*) + b_{nm}^{kl} \operatorname{Im} (\epsilon_n \epsilon_{n+1} \epsilon_m^* \epsilon_{m+1}^*), \quad (\text{B26})$$

where  $a_{nm}^{kl} = \operatorname{Re} (t_{kn} t_{ln+1} t_{km}^* t_{lm+1}^*)$  and  $b_{nm}^{kl} = \operatorname{Im} (t_{kn} t_{ln+1} t_{km}^* t_{lm+1}^*)$ . It is useful to expand the four epsilon interaction

$$\begin{aligned} \operatorname{Re} (4\epsilon_n \epsilon_{n+1} \epsilon_m \epsilon_{m+1}) &= 1 + \sigma_n \sigma_m + \sigma_n \sigma_{m+1} + \sigma_{n+1} \sigma_m + \sigma_{n+1} \sigma_{m+1} - \sigma_n \sigma_{n+1} - \sigma_m \sigma_{m+1} - \sigma_n \sigma_{n+1} \sigma_m \sigma_{m+1} \\ \operatorname{Im} (4\epsilon_n \epsilon_{n+1} \epsilon_m \epsilon_{m+1}) &= \sigma_m + \sigma_{m+1} - \sigma_n - \sigma_{n+1} + \sigma_n \sigma_m \sigma_{m+1} - \sigma_{n+1} \sigma_m \sigma_{m+1} - \sigma_n \sigma_{n+1} \sigma_m + \sigma_n \sigma_{n+1} \sigma_{m+1}. \end{aligned} \quad (\text{B27})$$

We see that the coincidences between mode  $k$  and  $l$  written with terms of constants, one spin, two spins, three spins and four spins,

$$\Gamma_{kl} = C^{kl} + T_{\sigma}^{kl} + T_{\sigma^2}^{kl} + T_{\sigma^3}^{kl} + T_{\sigma^4}^{kl}, \quad (\text{B28})$$

where,

$$C^{kl} = \frac{\alpha^2}{4} \sum_{nm} a_{nm}^{kl}, \quad (\text{B29})$$

$$\begin{aligned} T_{\sigma}^{kl} &= \sum_{nm} \alpha d_{nm}^{kl} \sigma_n + \frac{\alpha^2}{4} b_{nm}^{kl} (\sigma_m + \sigma_{m+1} - \sigma_n - \sigma_{n+1}) \\ &= \sum_{nm} \alpha d_{nm}^{kl} \sigma_n, \end{aligned} \quad (\text{B30})$$

where the last term cancels out due to the symmetry of  $b$ ,  $b_{nm}^{kl} = b_{mn}^{kl}$ .

$$\begin{aligned} T_{\sigma^2}^{kl} &= \sum_{nm} \alpha c_{nm}^{kl} (\sigma_n \sigma_m + \sigma_n \sigma_{m+1}) + \frac{\alpha^2}{4} a_{nm}^{kl} (\sigma_n \sigma_m + \sigma_n \sigma_{m+1} + \sigma_{n+1} \sigma_m + \sigma_{n+1} \sigma_{m+1} - \sigma_n \sigma_{n+1} - \sigma_m \sigma_{m+1}) \\ &= \sum_{nm} \alpha c_{nm}^{kl} (\sigma_n \sigma_m + \sigma_n \sigma_{m+1}) + \frac{\alpha^2}{4} a_{nm}^{kl} (\sigma_n \sigma_m + 2\sigma_n \sigma_{m+1} + \sigma_{n+1} \sigma_{m+1} - 2\sigma_n \sigma_{n+1}), \end{aligned} \quad (\text{B31})$$

where terms can be grouped because of the symmetry of  $a$ ,  $a_{nm}^{kl} = a_{mn}^{kl}$ . This term can be written as the spin-glass Hamiltonian,

$$T_{\sigma^2}^{kl} = \sum_{nm} J_{nm}^{kl} \sigma_n \sigma_m, \quad (\text{B32})$$

where  $J_{nm}^{kl} = \alpha c_{nm}^{kl} + \alpha c_{nm-1}^{kl} + \frac{\alpha^2}{4} a_{nm}^{kl} (1 - 2\delta_{m+1-n}) + \frac{\alpha^2}{2} a_{nm-1}^{kl} + \frac{\alpha^2}{4} a_{n-1m-1}^{kl}$ .

$$\begin{aligned} T_{\sigma^3}^{kl} &= - \sum_{nm} \alpha d_{nm}^{kl} \sigma_n \sigma_m \sigma_{m+1} - \frac{\alpha^2}{4} b_{nm}^{kl} (\sigma_{n+1} \sigma_m \sigma_{m+1} - \sigma_n \sigma_{n+1} \sigma_m - \sigma_n \sigma_{n+1} \sigma_{m+1}) \\ &= - \sum_{nm} \alpha d_{nm}^{kl} \sigma_n \sigma_m \sigma_{m+1} - \frac{\alpha^2}{4} b_{nm}^{kl} \sigma_n \sigma_{n+1} \sigma_{m+1} \\ &= - \sum_{nmp} \Lambda_{nmp}^{kl} \sigma_n \sigma_m \sigma_p, \end{aligned} \quad (\text{B33})$$

where we have used the symmetry of  $b$ ,  $b_{nm}^{kl} = b_{mn}^{kl}$ , and have defined  $\Lambda_{nmp}^{kl} = \left( \alpha d_{nm}^{kl} + \frac{\alpha^2}{4} b_{nm}^{kl} \right) \delta_{m+1-p}$ . And the last term writes,

$$\begin{aligned} T_{\sigma^4}^{kl} &= \frac{\alpha^2}{4} \sum_{mn} a_{nm}^{kl} \sigma_n \sigma_m \sigma_{n+1} \sigma_{m+1} \\ &= \sum_{nmpq} Q_{nmpq}^{kl} \sigma_n \sigma_m \sigma_p \sigma_q, \end{aligned} \quad (\text{B34})$$

where we have defined  $Q_{nmpq}^{kl} = \frac{\alpha^2}{4} a_{nm}^{kl} \delta_{n+1-p} \delta_{m+1-q}$ .

It should be noted that terms  $T_{\sigma^2}^{kl}$ ,  $T_{\sigma^3}^{kl}$  and  $T_{\sigma^4}^{kl}$  contain constant—with respect to the spins—when  $n = m$  or  $n = m+1$ . These terms can be absorbed into the constant term  $C^{kl}$ .

In our work we do not directly optimize  $\Gamma_{kl}$ , but  $\Gamma_T^+ = \sum_{k=1}^M \Gamma_{T+k, T-k}$ , which corresponds to an arbitrary pixel  $T$  of the sum-coordinate projection of  $\Gamma$ . Using Equation (B28),  $\Gamma_T^{(+)}$  is then expressed as:

$$\Gamma_T^+ = C^T - \frac{1}{2} \sum_n K_n^T - \frac{1}{2} \sum_n J_{nm}^T \sigma_n \sigma_m - \frac{1}{2} \sum_n \Lambda_{nml}^T \sigma_n \sigma_m \sigma_l - \frac{1}{2} \sum_n Q_{nmlp}^T \sigma_n \sigma_m \sigma_l \sigma_p, \quad (\text{B35})$$

where  $C^T = \sum_{k=1}^M C^{T+k, T-k}$ ,  $K_n^T = \sum_{k=1}^M K_n^{T+k, T-k}$ ,  $J_{nm}^T = \sum_{k=1}^M J_{nm}^{T+k, T-k}$ ,  $\Lambda_{nml}^T = \sum_{k=1}^M \Lambda_{nml}^{T+k, T-k}$  and  $Q_{nmlp}^T = \sum_{k=1}^M Q_{nmlp}^{T+k, T-k}$ . This result is Equation (4) of the manuscript.

In addition, it is interesting to note that if  $\alpha = 0$ , which corresponds to the case where the size of a SLM macropixel

is much larger than the position correlation width  $\sigma_{\mathbf{r}}$  of the photon pairs in the SLM plan, then Equation (4) of the manuscript simplifies into:

$$\Gamma_T^\pm = -\frac{1}{2} \sum_n \left( \sum_{kl} \text{Re}(t_{(T+k)n} t_{(T-k)n} \bar{t}_{(T+k)m} \bar{t}_{(T-k)m}) \right) \sigma_n \sigma_m, \quad (\text{B36})$$

That is the Hamiltonian of a conventional spin-glass model with only spin-spin interaction, similar to those obtained with classical optical Ising machines [6]. Finally, as explained in supplementary section VII A, it is also important to note that the approximation  $\psi_{mn}^{(i)} \approx \delta_{m-n} + \alpha \delta_{m-n+1}$  assumes a one-dimensional SLM i.e. the coefficient  $\alpha$  only creates coupling between one direct neighboring SLM macropixel. However, in reality, since the SLM is bidimensional, each SLM macropixel couples with 8 neighboring pixels, meaning that additional terms should be included. As a result, the coefficients  $C^T$ ,  $K_n^T$ ,  $J_{nm}^T$ ,  $\Lambda_{nml}^T$ , and  $Q_{nmlp}^T$  would be modified accordingly, but the model would still retain a structure with multi-spin interactions  $\sigma_n \sigma_m \sigma_l$  and  $\sigma_n \sigma_m \sigma_l \sigma_p$ , which is the key aspect of our demonstration.